



Ships Passing in the Night: Spectroscopic Analysis of Two Ultra-faint Satellites in the Constellation Carina^{*†‡}

T. S. Li^{1,2} , J. D. Simon³ , A. B. Pace^{4,29} , G. Torrealba⁵ , K. Kuehn⁶ , A. Drlica-Wagner¹ , K. Bechtol⁷ , A. K. Vivas⁸ , R. P. van der Marel^{9,10} , M. Wood^{11,12,13} , B. Yanny¹ , V. Belokurov¹⁴ , P. Jethwa¹⁵ , D. B. Zucker^{16,17} , G. Lewis¹⁸ , R. Kron^{1,19} , D. L. Nidever²⁰ , M. A. Sánchez-Conde^{21,22} , A. P. Ji^{3,30} , B. C. Conn²³ , D. J. James²⁴ , N. F. Martin^{25,26} , D. Martinez-Delgado²⁷ , and N. E. D. Noël²⁸

(MagLiteS Collaboration)

¹ Fermi National Accelerator Laboratory, P.O. Box 500, Batavia, IL 60510, USA; tingli@fnal.gov

² Kavli Institute for Cosmological Physics, University of Chicago, Chicago, IL 60637, USA

³ Observatories of the Carnegie Institution for Science, 813 Santa Barbara St., Pasadena, CA 91101, USA

⁴ George P. and Cynthia Woods Mitchell Institute for Fundamental Physics and Astronomy, and Department of Physics and Astronomy, Texas A&M University, College Station, TX 77843, USA

⁵ Institute of Astronomy and Astrophysics, Academia Sinica, P.O. Box 23-141, Taipei 10617, Taiwan

⁶ Australian Astronomical Observatory, North Ryde, NSW 2113, Australia

⁷ Large Synoptic Survey Telescope, 950 North Cherry Avenue, Tucson, AZ 85721, USA

⁸ Cerro Tololo Inter-American Observatory, National Optical Astronomy Observatory, Casilla 603, La Serena, Chile

⁹ Space Telescope Science Institute, 3700 San Martin Drive, Baltimore, MD 21218, USA

¹⁰ Center for Astrophysical Sciences, Department of Physics & Astronomy, Johns Hopkins University, Baltimore, MD 21218, USA

¹¹ Kavli Institute for Particle Astrophysics & Cosmology, P.O. Box 2450, Stanford University, Stanford, CA 94305, USA

¹² SLAC National Accelerator Laboratory, Menlo Park, CA 94025, USA

¹³ Department of Physics, Stanford University, 382 Via Pueblo Mall, Stanford, CA 94305, USA

¹⁴ Institute of Astronomy, University of Cambridge, Madingley Road, Cambridge CB3 0HA, UK

¹⁵ European Southern Observatory, Karl-Schwarzschild-Str. 2, D-85748 Garching, Germany

¹⁶ Department of Physics & Astronomy, Macquarie University, Sydney, NSW 2109, Australia

¹⁷ Australian Astronomical Observatory, 105 Delhi Rd, North Ryde, NSW 2113, Australia

¹⁸ Sydney Institute for Astronomy, School of Physics, A28, The University of Sydney, NSW 2006, Australia

¹⁹ Department of Astronomy and Astrophysics, University of Chicago, Chicago, IL 60637, USA

²⁰ National Optical Astronomy Observatory, 950 N. Cherry Avenue, Tucson, AZ 85719, USA

²¹ Instituto de Física Teórica UAM/CSIC, Universidad Autónoma de Madrid, E-28049 Madrid, Spain

²² Departamento de Física Teórica, M-15, Universidad Autónoma de Madrid, E-28049 Madrid, Spain

²³ Research School of Astronomy & Astrophysics, Mount Stromlo Observatory, Cotter Road, Weston Creek, ACT 2611, Australia

²⁴ Event Horizon Telescope, Harvard-Smithsonian Center for Astrophysics, 60 Garden Street, Cambridge, MA 02138, USA

²⁵ Université de Strasbourg, CNRS, Observatoire astronomique de Strasbourg, UMR 7550, F-67000 Strasbourg, France

²⁶ Max-Planck-Institut für Astronomie, Königstuhl 17, D-69117 Heidelberg, Germany

²⁷ Astronomisches Rechen-Institut, Zentrum für Astronomie der Universität Heidelberg, Mönchhofstr. 12-14, D-69120 Heidelberg, Germany

²⁸ Department of Physics, University of Surrey, Guildford GU2 7XH, UK

Received 2018 February 19; revised 2018 March 9; accepted 2018 March 10; published 2018 April 25

Abstract

We present Magellan/IMACS, Anglo-Australian Telescope/AAOmega+2dF, and Very Large Telescope/GIRAFFE+FLAMES spectroscopy of the Carina II (Car II) and Carina III (Car III) dwarf galaxy candidates, recently discovered in the Magellanic Satellites Survey (MagLiteS). We identify 18 member stars in Car II, including two binaries with variable radial velocities and two RR Lyrae stars. The other 14 members have a mean heliocentric velocity $v_{\text{hel}} = 477.2 \pm 1.2 \text{ km s}^{-1}$ and a velocity dispersion of $\sigma_v = 3.4^{+1.2}_{-0.8} \text{ km s}^{-1}$. Assuming Car II is in dynamical equilibrium, we derive a total mass within the half-light radius of $1.0^{+0.8}_{-0.4} \times 10^6 M_{\odot}$, indicating a mass-to-light ratio of $369^{+309}_{-161} M_{\odot}/L_{\odot}$. From equivalent width measurements of the calcium triplet lines of nine red giant branch (RGB) stars, we derive a mean metallicity of $[\text{Fe}/\text{H}] = -2.44 \pm 0.09$ with dispersion $\sigma_{[\text{Fe}/\text{H}]} = 0.22^{+0.10}_{-0.07}$. Considering both the kinematic and chemical properties, we conclude that Car II is a dark-matter-dominated dwarf galaxy. For Car III, we identify four member stars, from which we calculate a systemic velocity of $v_{\text{hel}} = 284.6^{+3.4}_{-3.1} \text{ km s}^{-1}$. The brightest RGB member of Car III has a metallicity of $[\text{Fe}/\text{H}] = -1.97 \pm 0.12$. Due to the small size of the Car III spectroscopic sample, we cannot conclusively determine its nature. Although these two systems have the smallest known physical separation ($\Delta d \sim 10 \text{ kpc}$) among Local Group satellites, the large difference in their systemic velocities, $\sim 200 \text{ km s}^{-1}$, indicates that they are unlikely to be a bound pair. One or both systems are likely associated with the Large Magellanic Cloud (LMC), and may remain

* This paper includes data gathered with the 6.5 m Magellan Telescopes located at Las Campanas Observatory, Chile.

† This paper includes data gathered with Anglo-Australian Telescope in Australia.

‡ Based on data products from observations made with ESO Telescopes at the La Silla Paranal Observatory under programme ID 298.B-5027.

²⁹ Mitchell Astronomy Fellow.

³⁰ Hubble Fellow.

LMC satellites today. No statistically significant excess of γ -ray emission is found at the locations of Car II and Car III in eight years of *Fermi*-LAT data.

Key words: dark matter – galaxies: dwarf – galaxies: individual (Carina II, Carina III) – galaxies: stellar content – Local Group – stars: abundances

Supporting material: machine-readable table

1. Introduction

The standard cosmological model with cold dark matter predicts that structure forms hierarchically over a wide range of size scales. The two most prominent satellites of the Milky Way, the Large and Small Magellanic Clouds (LMC and SMC), are both sufficiently massive to expect that they hosted their own populations of luminous satellites prior to their arrival at the Milky Way (D’Onghia & Lake 2008; Sales et al. 2011; Dooley et al. 2017). Indeed, the spatial distribution of the newly discovered ultra-faint dwarf galaxies in the Dark Energy Survey (DES; Abbott et al. 2005) is heavily biased toward the direction of the LMC and SMC, providing strong but indirect observational evidence for the existence of “satellites of satellites” around our Milky Way (Bechtol et al. 2015; Deason et al. 2015; Drlica-Wagner et al. 2015b; Koposov et al. 2015; Jethwa et al. 2016; Sales et al. 2017). Motivated by this distinct anisotropy in the southern satellite distribution, the Magellanic Satellites Survey (MagLiteS) is imaging the unexplored area on the other side of the Magellanic Clouds with the Dark Energy Camera (DECam; Flaugher et al. 2015) on the Blanco 4 m telescope at Cerro Tololo Inter-American Observatory. MagLiteS is described in more detail by Drlica-Wagner et al. (2016).

Recently, a pair of dwarf galaxy candidates located on the outskirts of the LMC were discovered using photometric data from MagLiteS: Carina II (Car II) and Carina III (Car III) (Torrealba et al. 2018, hereafter Paper I). These two systems are both extremely faint and close to us, with absolute magnitudes of $M_V \sim -4.5$ and $M_V \sim -2.4$, and heliocentric distances of $d \sim 37$ kpc and $d \sim 28$ kpc, respectively. Car II ($r_{1/2} \sim 90$ pc) is significantly more extended than Car III ($r_{1/2} \sim 30$ pc). Remarkably, these two objects form a close pair both on the sky (where they have a projected separation of $18'$, or ~ 150 pc at $d \sim 28$ kpc) and along the line of sight (where they are ~ 10 kpc apart), raising the question of whether Car II and Car III are gravitationally bound. Furthermore, due to the proximity of both systems to the LMC (~ 18 kpc from Car II and ~ 25 kpc from Car III), it seems likely that one or both are (or were) physically associated with the Magellanic Clouds. Kinematic information, such as line-of-sight velocities, is necessary to address these hypotheses, and confirm the nature of the two systems.

Soon after the initial discovery in 2016 December, we began a spectroscopic follow-up program with the Magellan Baade Telescope, the Anglo-Australian Telescope (AAT), and the Very Large Telescope (VLT). Rapid follow-up with the AAT and VLT was possible thanks to short turn-around time for approval of service observations and Director’s Discretionary time. Our multi-pronged observational strategy enabled both deep observations of a smaller number of faint targets with the 8 m class Magellan and VLT, and wider-field observations of a large number of brighter targets (in both Car II and Car III together) with the AAT.

Here, we report the first spectroscopic analysis of the Car II and Car III dwarf galaxy candidates discovered in MagLiteS.

In Section 2, we describe the observations with all three telescopes, and the data reduction procedures. In Section 3, we detail the results from our spectroscopic program, including the set of spectroscopic members, and measurements of the radial velocity, velocity dispersion, mean metallicity, and metallicity dispersion for each dwarf galaxy candidate. In Section 4, we discuss the implications of these derived parameters as they relate to the classification of Car II and Car III, along with other unique features of this pair—specifically, the possible tidal interaction between the two systems, and the association of Car II and Car III with the Magellanic Clouds. We also briefly discuss the search for dark matter annihilation within the Carina systems. We conclude in Section 5.

The photometry in this work has been dereddened using the Schlegel et al. (1998) extinction map around Car II and Car III. Because of the relatively low Galactic latitude, the average reddening in this region is $E(B - V) \sim 0.19$.

2. Observations and Data Reduction

2.1. Magellan/IMACS Spectra

We obtained multi-slit spectroscopy of Car II and Car III with the IMACS spectrograph (Dressler et al. 2006) on the Magellan Baade telescope on 2017 January 24–25. The observing setup was the same as for the spectroscopy of the Tucana III (Simon et al. 2017) and Eridanus II (Li et al. 2017) dwarf galaxies. We used the $f/4$ camera on IMACS, which provides a full field-of-view of $15'.4 \times 15'.4$. The spectrograph was configured with the 1200 ℓ /mm grating and a tilt angle of $32^\circ.4$, producing a spectral resolution of $R \sim 11,000$ for a $0''.7$ slit width and a wavelength range of at least 7550–8750 Å for each slit. This wavelength range covers the calcium triplet (CaT) lines around 8500 Å, used for measuring radial velocities and metallicities of candidate member stars, as well as the telluric absorption lines (Fraunhofer A-band) around 7600 Å used for the correction of velocity errors caused by mis-centering of the stars within the slits (see Sohn et al. 2007 for details).

The target selection and mask design for Magellan/IMACS (hereafter IMACS) were performed using the photometry from the original MagLiteS catalog. Based on the knowledge of confirmed members of the DES-discovered dwarf galaxies Reticulum II from Simon et al. (2015) and Tucana III from Simon et al. (2017), we used similar selection criteria as described in the latter paper. Target selection and mask design used a preliminary estimate for the distance modulus for Car II (Car III) of $m - M = 17.5$ ($m - M = 17.1$). For Car II, the red giant branch (RGB) candidate members were selected to be redder than the fiducial sequence of the metal-poor globular cluster M92 from An et al. (2008), bluer than a 12 Gyr, $[\text{Fe}/\text{H}] = -2.2$ theoretical PARSEC isochrone³¹ from Bressan et al. (2012), and brighter than $g = 20.8$. Several candidate blue horizontal branch (BHB) stars were selected at $17.7 < g <$

³¹ Note that an earlier version of the PARSEC isochrone was used. See the Appendix for more details regarding the updated PARSEC isochrones.

18.8 and $g - r < 0.1$; a handful of candidate red horizontal branch (RHB) stars were selected at $17.9 < g < 18.6$ and $0.1 < g - r < 0.3$. Potential main sequence turnoff (MSTO) stars were selected using a 0.1 mag wide window in $g - r$ around the PARSEC isochrone for $20.8 < g < 22$ (although because of the observing conditions, we did not get any useful spectra for MSTO candidates).

For Car III, we used the same selection criteria as for Car II, with the exception of shifting all sequences 0.4 mag brighter according to the difference in distance moduli. Based on these targets, we designed two slitmasks (IMACS-Car2Mask1 and IMACS-Car2Mask2) near the center of Car II and one slitmask (IMACS-Car3Mask1) near the center of Car III, using the maskgen program.³² Stars were placed on the slit masks in a category prioritization descending order of BHB, RGB, RHB, and MSTO. Within each category, priorities were based on brightness and distance from the center of Car II or Car III. Finally, any remaining mask space was filled by stars with photometry that made them unlikely to be members. IMACS-Car2Mask1 contains 72 slits, IMACS-Car2Mask2 contains 48 slits, and IMACS-Car3Mask1 contains 67 slits. All the targets, observed with IMACS and other instruments described in later sections, are presented in Figure 1.

We obtained a 1.7 hr exposure with IMACS-Car2Mask2 and a 3.7 hr exposure with IMACS-Car3Mask1 on 2017 January 24, and a 1.25 hr exposure on IMACS-Car2Mask1 on 2017 January 25. One of the BHB candidates, MAGLITES J073834.84–575211.2, on IMACS-Car3Mask1 happened to fall in a gap between CCDs, so we also obtained a 30 minute exposure on this star with a 0"7-wide long slit (IMACS-Car3LongSlit) on 2017 January 25. The observing conditions on both nights were relatively poor, with high humidity and $\sim 1''$ – $3''$ seeing.

We reduced the IMACS spectra following the procedures described by Simon et al. (2017) for Tucana III. We first performed the bias subtraction and removal of read-out pattern noise, then we used the Cosmos pipeline (Dressler et al. 2011; Oemler et al. 2017) to derive an initial wavelength solution and performed the slit mapping, followed by a refined wavelength calibration and spectral extraction using an IMACS pipeline derived from the DEEP2 data reduction pipeline for Keck/DEIMOS (Cooper et al. 2012). For each mask, the extracted spectra from multiple exposures were combined using inverse-variance weighting. The combined spectra reach a signal-to-noise ratio (S/N) $\sim 5 \text{ pixel}^{-1}$ at $r = 19.0$ for Car II and at $r = 19.3$ for Car III.

The details of the instrument setup, observing information, mask information, etc., for IMACS and other instruments described in later sections, are summarized in Table 1.

2.2. AAT/AAOmega+2dF Spectra

We observed Car II and Car III with the AAOmega Spectrograph (Sharp et al. 2006), a fiber-fed multi-object spectrograph on the 3.9 m AAT at the Australian Astronomical Observatory (AAO). The AAOmega Spectrograph is fed by the Two Degree Field ("2dF") multi-object system, allowing acquisition of up to 392 simultaneous spectra of objects within a 2° field on the sky.

AAOmega is a dual-beam spectrograph, which feeds a blue arm and a red arm with a beam splitter at 5700 Å. For the red

arm, we utilized the 1700D grating, providing a spectral resolution of $R = 10,000$ and wavelength coverage of 8400–8810 Å, which enabled us to target the spectral region of the CaT absorption lines for velocity and metallicity measurements. For the blue arm, we chose the 580V grating with resolution of $R = 1300$ and wavelength coverage of 3750–5750 Å, which allowed us to study additional elements (e.g., carbon) in the blue. This paper focuses on the kinematics and metallicities of the Carina systems, and therefore the spectra from the blue arm will be discussed in a future paper.

Observations with AAT/AAOmega+2dF (hereafter AAT) were taken on 2017 January 23 and May 29 through the service observing program, and on 2017 January 25 through classical observing time. We obtained three 40 minute exposures on January 23, one 40 minute exposure and one 60 minute exposure on January 25, and two 40 minute exposures on May 29. To ensure accurate velocity determination, the arc frames were taken right before the science exposures at the same position. During the January run, the seeing was around $1''$ – $1.5''$ with intermittent clouds. During the May run, the weather was clear with seeing around $1.6''$ – $2.2''$. Among the 392 fibers, 25 of them were assigned to sky positions, eight were assigned to guide stars selected from the UCAC4 catalog (Zacharias et al. 2013), and the remaining fibers were assigned to target stars.

The targets for the AAT run were mostly selected using the photometry from the original MagLiteS catalog. The RGB and RHB candidates were selected using the best-fit PARSEC isochrone for Car II (log age = 10.0, [Fe/H] = -1.7 , $m - M = 17.5$) and Car III (log age = 9.75, [Fe/H] = -0.9 , $m - M = 17.1$) at the time of the observations.³³ The BHB candidates were selected using a fiducial M92 BHB isochrone placed at the distance modulus of Car II and Car III.

In addition to MagLiteS photometry, we also used photometry from time-series follow-up observations (to search for RR Lyrae stars) acquired with DECam during Blanco 4 m Director's Discretionary and engineering time. The exposure times for these follow-up studies were shorter than the original MagLiteS exposures and therefore brighter stars could be observed. In addition, u -band measurements were performed in the follow-up observations, and a handful of K/M giant candidates were selected based on the $u - g$ and $g - i$ color (e.g., see Figure 2 of Yanny et al. 2009). Furthermore, we included some RR Lyrae candidates from the preliminary analysis of time-series follow-up studies. Thanks to the proximity of Car II and Car III on the sky, as well as the large field of view (FOV) of AAT+2dF, both systems were targeted in a single pointing. We assigned RR Lyrae candidates the highest priority, followed by the BHB and K/M giant candidates. Stars in two remaining categories (RGB, RHB) were prioritized based on their brightness in the r -band. Note that the target spacing of 2dF is typically $30''$ – $40''$ due to fiber collisions, and therefore some targets located close to the centers of Car II and Car III were missed where the target density is high.

The candidate stars were then allocated according to the priorities described above using the fiber configuration program `configure`³⁴ provided by the AAO. Flexibility in target allocation

³² <http://code.obs.carnegiescience.edu/maskgen>

³³ Note that the final isochrone parameter values reported in Paper I are different from those used for spectroscopic target selection because the photometry and the fits continued to be refined after the spectroscopic observations were obtained.

³⁴ <https://www.aao.gov.au/science/software/configure>

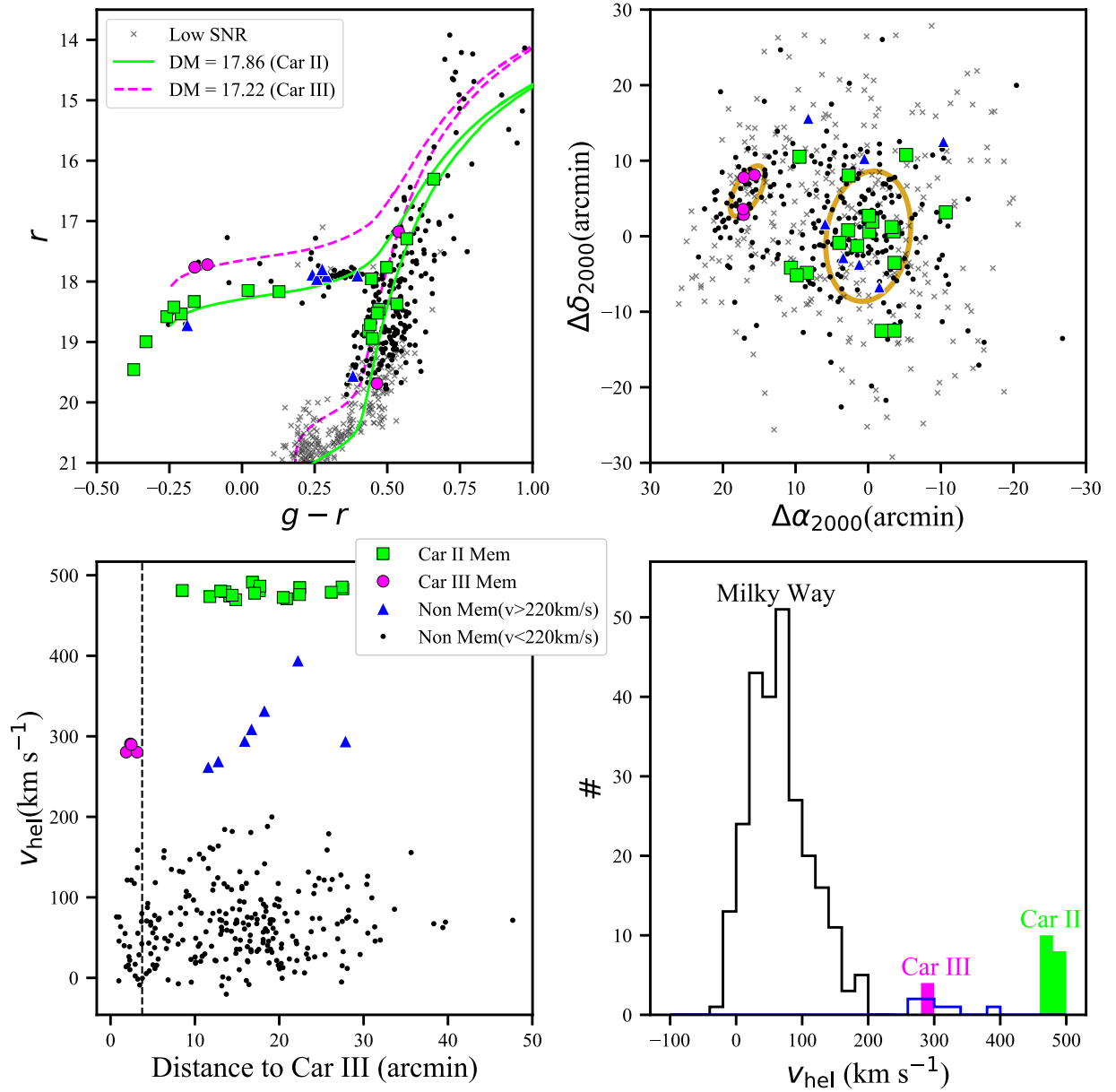


Figure 1. Upper left: color-magnitude diagram for observed stars with Magellan/IMACS, AAT/2dF+AAOmega, and VLT/GIRAFFE+FLAMES. Overplotted are the PARSEC isochrones of a metal-poor population with age = 12.0 Gyr, $[\text{Fe}/\text{H}] = -2.2$ at the distance of Car II ($m - M = 17.86$, green) and Car III ($m - M = 17.22$, magenta). Green squares indicate 18 members of Car II, magenta circles indicate four members of Car III, blue triangles indicate seven non-members with velocities $v_{\text{hel}} > 220 \text{ km s}^{-1}$, and small black dots are remaining non-members with velocities $v_{\text{hel}} < 220 \text{ km s}^{-1}$; black cross markers indicate candidate members that were observed but for which we were unable to obtain velocity measurements (mainly due to low signal-to-noise ratio). Upper right: spatial distribution of the targets. Gold ellipses show the half-light radius of Car II (larger ellipse) and Car III (smaller ellipse). Lower left: heliocentric velocity vs. distance from the center of Car III. The separation between the Car II members, Car III members and the non-members is obvious. A few non-members have velocities similar to that of Car III, but are far away from the Car III center. The black dashed line indicates the half-light radius of Car III ($r_h = 3.75$; Paper I). Lower right: velocity distribution of 283 stars with successful velocity measurements. Car II members are indicated as the peak around 480 km s^{-1} (in green) and Car III members are indicated as the peak around 280 km s^{-1} (in magenta). A few stars have velocities close to Car III and are shown as a blue histogram. From their position on the sky (upper-right panel) and their distance from Car III (lower-left panel) we conclude that they are not members of Car III.

with 2dF allowed us to identify bright ($S/N > 20$ per pixel) non-member stars in the January 23 data, leading to re-allocation of those fibers to alternative targets during the January 25 observations. A total of 388 candidates were targeted from the two nights of observations in the January run; 309 of them were targeted again in the May run.

The data reduction was performed using the `2dfdr`³⁵ v6.28 data reduction program of the AAO. The reduction includes

bias subtraction, scattered light subtraction, flat-fielding, optimal spectral extraction, wavelength calibration, sky subtraction, and frame combination with cosmic ray rejection. Wavelength calibration was first performed using the arc frames taken immediately before or after each science exposure, followed by a recalibration with a second-order polynomial fit using sky emission lines. As the observations were taken from different nights, the reduced spectra were corrected for the heliocentric motion of the Sun at each exposure, before the spectra from multiple exposures were

³⁵ <https://www.aao.gov.au/science/software/2dfdr>

Table 1
Observations

Mask/Run Name	α (J2000) (h m s)	δ (J2000) ($^{\circ}$ ' ")	Slit PA (deg)	$\lambda/\Delta\lambda$	disp. Å/pix	# of Exp	Σt_{exp} (s)	Seeing (")	MJD ^a	# of Slits/Fibers	# of Useful Spectra
IMACS-Car2Mask1	07:36:36.00	-57:57:20.0	172.0	11,000	0.19	2	4500	1"2	57779.3	72	32
IMACS-Car2Mask2	07:36:26.00	-58:02:00.0	248.0	11,000	0.19	3	6000	1"5	57778.3	48	33
IMACS-Car3Mask1	07:38:28.00	-57:53:30.0	317.0	11,000	0.19	6	13200	2"5	57778.2	67	40
IMACS-Car3LongSlit	07:38:34.84	-57:52:11.2	180.0	11,000	0.19	1	1800	1"2	57779.3	1	1
AAT-Jan	07:36:33.60	-58:01:12.0	...	10,000	0.24	5	13200	1"3	57777.6	388	131
AAT-May	07:36:33.60	-58:01:12.0	...	10,000	0.24	2	4800	2"0	57902.4	309	55
VLT-Feb	07:37:32.40	-57:57:16.0	...	6,000	0.20	1	2775	0"3	57811.1	116	116

Note.

^a The date listed here is the weighted mean observation date over multiple exposures. For AAT-Jan observations, the date is the weighted mean over multiple nights.

combined using inverse-variance weighting. To detect possible binary stars, we combined the spectra from the January run (AAT-Jan) and May run (AAT-May) separately for the velocity measurements. The combined spectra had S/N $\sim 5 \text{ pixel}^{-1}$ at $r = 18.7$ for AAT-Jan and at $r = 18.0$ for AAT-May.

2.3. VLT/GIRAFFE+FLAMES Spectra

After the observations with AAT and Magellan, we also observed Car II and Car III with the GIRAFFE+FLAMES spectrograph (Pasquini et al. 2000) on the 8.2 m Kueyen telescope (UT2) based at the ESO-VLT through Director's Discretionary time. Observations were taken in MEDUSA mode, which allows the simultaneous observation of up to 132 objects, with a minimum target separation of 11" due to fiber collisions. On the night of 2017 February 26, one 2775 s exposure was taken under excellent seeing conditions ($\sim 0"3$). The LR8 grating was used for this observation, which covers the wavelength range from 8206 to 9400 Å at a resolution of $R \sim 6000$. The calibration frames, including biases, flats and ThAr arcs, were taken at the end of the night.

Target selection for VLT/GIRAFFE+FLAMES (hereafter VLT) was done in a similar way as for the AAT, with the exception that we manually shifted the best-fit PARSEC isochrone $g - r \sim 0.07$ bluer, based on the confirmed Car II members identified by IMACS and AAT.³⁶ As the FOV of FLAMES is about 25' in diameter, we centered the exposure field in between Car II and Car III and therefore missed some of the BHB members found in the AAT data (see Section 3). A total of 116 targets were selected to feed to FLAMES, with 13 fibers assigned to blank sky positions.

As only a single exposure was obtained with VLT, we first removed cosmic rays using L.A.Cosmic (van Dokkum 2001). We then reduced the data with the GIRAFFE Gasgano pipeline (v2.4.8) provided by ESO for bias subtraction, flat-fielding, wavelength calibration, and spectral extraction of individual objects. We performed a wavelength re-calibration using sky emission lines and a sky subtraction with our own code. For details, we refer to the spectroscopic analysis of the Horologium I dwarf galaxy (T. S. Li et al. 2018, in preparation). In summary, a first-order wavelength correction derived from sky lines was applied to every spectrum to compensate for the wavelength shift likely caused by the temperature changes between the science observing during

the night and the calibration frames taken at the end of the night. We then combined the 13 sky fibers into a master sky spectrum. To compensate for fiber-to-fiber throughput and resolution variations, for each target spectrum we degraded the resolution of either the target spectrum or the master sky spectrum (whichever had the higher resolution) and then scaled the master sky spectrum to match the intensity of the sky lines in the target spectrum before the subtraction. The final reduced spectra (referred to as VLT-Feb) had S/N $\sim 7 \text{ pixel}^{-1}$ at $r \sim 19.8$.

3. Results

In this section, we present the results derived from the observations taken from the three telescopes. We first determine the radial velocity of each individual candidate star. We then identify member stars based on the velocity, spatial location, and location on the color-magnitude diagram (CMD). After identifying the member stars, we also compute the systemic velocity, velocity dispersion, mean metallicity, and metallicity dispersion for Car II and Car III.

We use the distance moduli (dereddened) and structural parameters from Paper I for the analysis in this work, unless otherwise stated. These parameters, together with the derived quantities in this section, are summarized in Table 2. We note that in Paper I, the distance modulus of Car II was calculated independently from the RR Lyrae stars and the MSTO stars. The distance modulus derived from the RR Lyrae stars is adopted in this work since it has a smaller uncertainty.

3.1. Radial Velocity Measurements

The reduced spectra from IMACS, AAT, and VLT were used for radial velocity measurements following the method described in Li et al. (2017). We measured the heliocentric radial velocities (v_{hel}) by fitting the reduced spectra with velocity templates using a Markov chain Monte Carlo (MCMC) sampler and finding the best-fit velocity that maximizes the likelihood defined by Equation (1) in Li et al. (2017). Instead of using only one velocity template per spectrum, we defined a set of templates for each instrument and used the template that gave the largest likelihood at the best-fit velocity as the best template for each star. The template set for each instrument included at least one metal-rich RGB, one metal-poor RGB, and one BHB star. The velocity templates for AAT and IMACS were observed using the same instrument setting as the science observation and were constructed following the description in Simon et al. (2017). We were not able to obtain any velocity template spectra during

³⁶ The original PARSEC synthetic isochrones used an out-of-date DECam system response. See details about this shift in the Appendix.

Table 2
Summary of Properties of Carina II and Carina III^a

Row	Property	Carina II	Carina III
(1)	R.A. (J2000)	114.1066 ± 0.0070	114.6298 ± 0.0060
(2)	Decl. (J2000)	−57.9991 ± 0.0100	−57.8997 ± 0.0080
(3)	(<i>m</i> − <i>M</i>)	17.86 ± 0.02 ^b	17.22 ± 0.10
(4)	Heliocentric distance (kpc)	37.4 ± 0.4 ^b	27.8 ± 0.6
(5)	<i>M</i> _{V,0}	−4.5 ± 0.1	−2.4 ± 0.2
(6)	<i>L</i> _{V,0} (<i>L</i> _⊙)	5.4 ± 0.5 × 10 ³	7.8 ^{+1.6} _{−1.3} × 10 ²
(7)	<i>r</i> _{1/2} (arcmin)	8.69 ± 0.75	3.75 ± 1.00
(8)	<i>r</i> _{1/2} (pc)	91 ± 8	30 ± 9
(9)	<i>ε</i> = 1 − <i>b/a</i>	0.34 ± 0.07	0.55 ± 0.18
(10)	PA (N to E; deg)	170 ± 9	150 ± 14
(11)	Number of members	14 ^c	4
(12)	<i>v</i> _{hel} (km s ^{−1})	477.2 ± 1.2	284.6 ^{+3.4} _{−3.1}
(13)	<i>v</i> _{GSR} (km s ^{−1})	235	42
(14)	<i>σ_v</i> (km s ^{−1})	3.4 ^{+1.2} _{−0.8}	5.6 ^{+4.3} _{−2.1} ^d
(15)	<i>M</i> _{half} (<i>M</i> _⊙)	1.0 ^{+0.8} _{−0.4} × 10 ⁶	...
(16)	<i>M/L_V</i> (<i>M</i> _⊙ / <i>L</i> _⊙)	369 ⁺³⁰⁹ _{−161}	...
(17)	<i>dv/dχ</i> (km s ^{−1} arcmin ^{−1})	0.0 ± 0.3	...
(18)	Mean metallicity	−2.44 ± 0.09	−1.97 ^e
(19)	Metallicity dispersion (dex)	0.22 ^{+0.10} _{−0.07}	...
(20)	log ₁₀ <i>J</i> (0°1) (GeV ² cm ^{−5})	17.9 ^{+0.6} _{−0.5}	19.9 ^{+1.0d} _{−0.9}
(21)	log ₁₀ <i>J</i> (0°5) (GeV ² cm ^{−5})	18.2 ^{+0.5} _{−0.3}	20.2 ^{+1.0d} _{−0.9}
(22)	log ₁₀ <i>D</i> (0°1) (GeV cm ^{−2})	16.9 ^{+0.3} _{−0.3}	17.8 ^{+0.5d} _{−0.5}
(23)	log ₁₀ <i>D</i> (0°5) (GeV cm ^{−2})	18.0 ^{+0.4} _{−0.4}	18.8 ^{+0.6} _{−0.7} ^d

Notes.

^a Rows (1)–(10) are taken or derived from Paper I. Values in rows (11)–(23) are derived using the measurements in this paper. All values reported here (and in this paper) are from the 50th percentile of the posterior probability distributions. The uncertainties are from the 16th and 84th percentiles of the posterior probability distributions.

^b The distance derived from RR Lyrae in Paper I is listed here as the heliocentric distance of Car II and is used throughout the paper. For other quantities, parameters derived from the CMD fit are used instead.

^c There are 18 spectroscopic members but only the 14 non-variable stars are used for kinematic analysis.

^d Note that the velocity dispersion and the *J*-factor for Car III is calculated based on only four spectroscopic members. We caution against the use of this calculation as the classification of Car III is remain unclear.

^e Note that this is the metallicity of the brightest member in Car III and not the mean metallicity of the system.

the VLT run. Instead, we used the Keck/DEIMOS templates from Kirby et al. (2015a), as the Keck/DEIMOS spectra have a much wider wavelength coverage and a similar resolution (*R* ∼ 6000) as our VLT spectra. For the IMACS spectra, we also applied a telluric correction derived using a telluric template to correct for the mis-centering of spectroscopic targets within each slit (see Li et al. 2017 for more details).

The statistical uncertainty on each velocity measurement is calculated as the standard deviation of the posterior velocity distribution from the MCMC sampler. This error is related primarily to the S/N of the spectra, with stellar temperature and metallicity also playing a role. Other systematic effects, such as instrument flexure, uncertainties in the wavelength calibration,

uncertainties in the template velocity, and template mismatching should also be considered in the final velocity uncertainty budget. We estimated the systematic uncertainty as the quadrature difference between repeat measurements and the statistical uncertainty (see Li et al. 2017; Simon & Geha 2007; Simon et al. 2017). We adopted the systematic floor of 1.0 km s^{−1} for IMACS from Simon et al. (2017). For AAT, we determined the systematic floor to be 0.5 km s^{−1} using repeat measurements of 18 bright stars (S/N > 8) from the January run and the May run. Since only one exposure was taken with VLT, we were not able to derive a systematic floor with this data set. We adopted a systematic floor of 0.9 km s^{−1} from the VLT observations of Horologium I (T. S. Li et al. 2018, in preparation), which has the same instrument setup as this data set. We added these systematic uncertainties in quadrature with the statistical uncertainties to obtain the final reported velocity uncertainties δ_v .

In order to combine the velocities derived from three different spectrographs to produce the final data set for the velocity dispersion determination in Section 3.3, we need to verify that there is no systematic offset between these three data sets. We compare the repeated measurements from different instruments as shown in the top panels of Figure 2 and find no obvious systematic offset between any given pair of instruments. In order to confirm that our error estimation is reasonable for each instrument, we again use these repeated measurements from each pair of instruments and compute the distribution of velocity differences between the two independent measurements (*v*₁, *v*₂), divided by the quadrature sum of their uncertainties ($\sqrt{\delta_1^2 + \delta_2^2}$). The resulting distributions, shown in the bottom panels of Figure 2, are well-described by normal distributions with zero mean and unit variance, as shown by red dashed curves in the same plots. From this comparison, we conclude that there is no significant zero-point shift between the various spectrographs, and that combining the three data sets will not introduce additional velocity uncertainties.

In order to study the kinematics of Car II and Car III, as well as the spectroscopic membership in each system, we combined the velocity measurements from the three different instruments into a single data set. With this combined sample, we successfully determined the velocities of 283 stars. The heliocentric velocities and the associated uncertainties are reported in Table 4. Note that, although the results reported in the table are from each observing run or each mask, we use the weighted average ($w = 1/\delta^2$) for stars with more than one measurement for the remainder of this paper.

3.2. Spectroscopic Membership Determination

Figure 1 shows the CMD, spatial distribution, and velocity distribution of the observed stars in both systems. We identified a total of 18 members in Car II and four members in Car III from the combined sample (see below).

The 18 members in Car II form a coherent velocity peak near 480 km s^{−1} in the heliocentric velocity distribution (lower right panel), including six BHB members, two RR Lyrae members, and ten RGB members. Since the heliocentric velocity of Car II is quite high relative to the mean velocity and velocity dispersion of the Milky Way halo, there are no foreground contaminants anywhere near the velocity of Car II. Furthermore, all stars within this velocity peak fall on the Car II isochrone, making the membership of this system unambiguous. The BHB members are

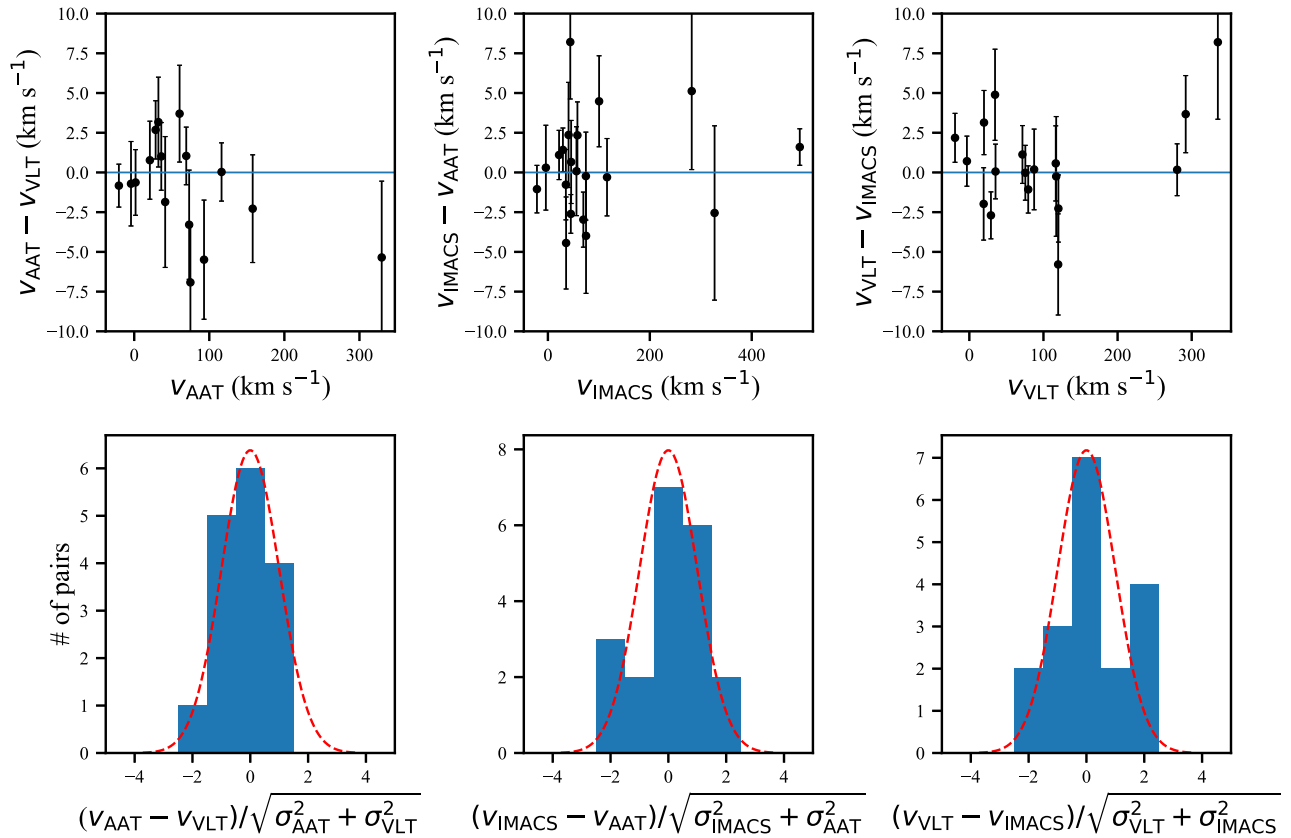


Figure 2. Top row: comparison of velocity measurements from different instruments using repeated measurements. There are no obvious zero-point shifts between three instruments. Bottom row: radial velocity uncertainty estimation tests using the repeated observations from different instruments. The histograms show the distributions of the velocity difference normalized by the quadrature sum of their uncertainties. The red dashed curves show a normal distribution with zero mean and unit variance scaled by the total number of pairs. The good agreement with the blue histograms indicates that our estimation of the velocity uncertainties is reasonable.

all far from the center of Car II ($r > 10'$) and therefore four of them are only observed with AAT. The velocity uncertainties of these BHB members are relatively large as a result of their broad lines and the low S/N of their spectra. The brightest RGB member, MAGLITES J073621.25–575800.3, was observed both in January (AAT and IMACS) and in May (AAT). The difference between the January and May observations is ~ 30 km s⁻¹. Another RGB member, MAGLITES J073646.47–575910.2, was observed both in January (AAT and IMACS) and February (VLT), and the difference is ~ 25 km s⁻¹. We therefore conclude that these two stars are binaries. The two RR Lyrae members of Car II also show velocity variability, and are discussed in more detail in Section 3.2.2.

We find a second narrow peak in the velocity distribution, containing four stars, centered at 280 km s⁻¹. All four stars are located within the Car III half-light radius and we therefore identify them as Car III members. While it is difficult to confirm an association based on only four stars, two of the four are BHB stars at the distance of Car III ($m - M = 17.22$, see the upper left panel in Figure 1). The brighter of the two RGB stars lies exactly on the expected Car III isochrone, while the fainter one is slightly redder than expected. Nevertheless, the combination of the spatial coincidence between these stars and their position in the CMD strongly suggests that this group is related to Car III.

Finally, seven candidate stars have velocities in the range 260–400 km s⁻¹ and are displayed in blue in Figure 1. Given their velocities, these stars are clearly not members of Car II. Their CMD positions and large distance away from Car III also

indicate that they are not Car III members. We used the Besançon Galactic stellar model (Robin et al. 2003) to estimate the expected number of foreground Milky Way stars in our spectroscopic sample. We selected simulated stars within 0.2 mag of the PARSEC isochrone and with $r < 19.5$. We found that in an area of 1 deg² centered on Car II there are ~ 15 simulated stars that have a velocity larger than 260 km s⁻¹, with a majority at $g - r < 0.4$ (i.e., foreground main-sequence stars). The surface density of non-Car II and Car III members in our spectroscopic sample is similar to this value. The small number of contaminants from the Besançon model further supports the conclusion that the two peaks are associated with Car II and Car III members. Given that Car II is relatively close to the LMC on the sky, some of these non-member stars might also belong to the LMC, which is discussed further in Section 3.2.1.

3.2.1. LMC Contamination

The field of Car II and Car III is located 18° from the center of the LMC, which corresponds to a 3D separation of ~ 18 kpc between Car II and the LMC, and of ~ 25 kpc between Car III and the LMC. While the visible body of the LMC is contained within the central $\sim 10^\circ$ (e.g., Besla et al. 2016), stars associated with the LMC have been detected as far out as $\sim 20^\circ$ (e.g., Nidever et al. 2017). Recently, Belokurov & Koposov (2016) also reported the detection of a small number of BHB candidates likely associated with the Magellanic Clouds, at a wide range of angular distances, extending out to

$\sim 30^\circ$ or perhaps even $\sim 50^\circ$ from the LMC. Interestingly, the diffuse cloud of BHB-like stars appears rather clumpy; the authors identify at least four individual stream-like structures. The most significant of these, the so-called S1 stream, can be traced securely to 20° – 25° from the LMC. Further support for the picture in which the LMC is enshrouded in a thin veil of stellar debris comes from the studies of Mackey et al. (2016) and Belokurov et al. (2017), who use main sequence and RR Lyrae stars, respectively, to trace a halo-like component around the LMC out to $\sim 20^\circ$ from its center. Finally, as Boubert et al. (2017) demonstrate using a combination of a stellar evolution code and N -body simulations of the LMC infall, the Cloud ought to be surrounded by an envelope of runaway stars. These high-velocity escapees are kicked out of the dwarf's disk during stellar binary disruption as a result of core-collapse supernova explosions, and can travel many tens of kpc away from the LMC in all directions.

It is therefore possible that some stars in our spectroscopic sample belong to the LMC. To calculate what the velocities of such stars might be, we used the rotating disk models of van der Marel & Sahlmann (2016). These imply that the line-of-sight velocity of the LMC disk at the sky position of Car II and Car III is 380 km s^{-1} . This is 118 km s^{-1} higher than the systemic velocity of the LMC center of mass, due to the fact that far from the center of the galaxy a significant component of its large transverse velocity vector projects along the line of sight. The locations of Car II and Car III are on the near side of the inclined LMC disk, so the heliocentric distance to the disk there is only 43.5 kpc. Since the positions of Car II and Car III are near the kinematic minor axis, a possible non-rotating LMC halo population would have more or less the same velocity (namely, 380 km s^{-1}) as the rotating disk. Old populations in the visible part of the LMC have velocity dispersions in the range 20 – 30 km s^{-1} (van der Marel et al. 2009). van der Marel et al. (2002) also show that the velocity dispersion is almost a constant of $\sim 20 \text{ km s}^{-1}$ between 2 and 9 kpc from the LMC center. We expect the dispersion at the position of Car II and Car III (~ 20 kpc from LMC) to be similar, though it largely depends on the mass and extent of the LMC's dark halo. Moreover, the tidal radius of the LMC is 24.0 ± 5.6 (van der Marel & Kallivayalil 2014). Therefore, tidal perturbations could affect both the mean velocity and velocity dispersion of LMC stars at the positions of Car II and Car III.

The mean velocities inferred here for Car II and Car III are offset by $\sim \pm 100 \text{ km s}^{-1}$, respectively, from the predicted velocities of LMC members. Therefore, contamination by LMC members at the Car II and Car III velocities is expected to be negligible. We do detect seven non-member stars (triangles in Figure 1; see also Table 4) with v_{hel} in the range 260 – 400 km s^{-1} . These velocities correspond to much smaller velocities in the Galactocentric frame (~ 40 – 180 km s^{-1}), since Car II and Car III are located almost opposite from the direction of solar motion. Among these seven stars, six have $0.2 < g - r < 0.4$ and are very likely to be foreground halo stars at much closer distances. The seventh star, MAGLITES J073634.86–580340.6, is a BHB star with $g - r \sim -0.2$. From the CMD (see the upper left panel in Figure 1), its distance is slightly farther than that of Car II. Comparing its r -band magnitude with the BHB members in Car II and Car III, we estimate the distance modulus of this star to be $m - M = 18.1 \pm 0.1$, corresponding to a heliocentric distance of $42 \pm 2 \text{ kpc}$, matching well with the model prediction of $\sim 43.5 \text{ kpc}$ for the near side of the LMC mentioned above. This

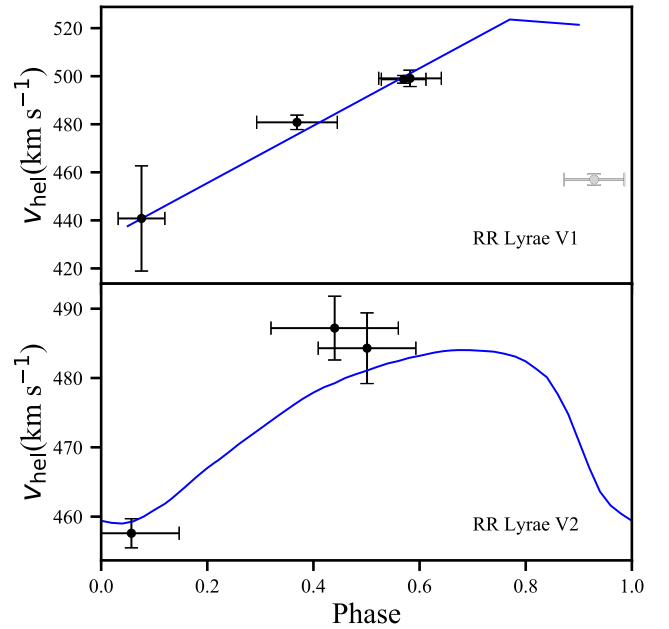


Figure 3. Radial velocity curve fits for the observations of the RR Lyrae stars MAGLITES J073637.00–580114.5 (V1, top) and MAGLITES J073645.86–575154.1 (V2, bottom). Circles represent the measurements from each individual spectrum, which were obtained at different phases during the pulsation cycle. The rightmost symbol (gray) for V1 (at phase 0.93) is shown only for reference but it was not used in the fitting of the radial velocity curve since it is located near a large discontinuity in the radial velocity curve. Error bars on the horizontal axis are not real errors but represent the time span (in units of phase) over which each spectrum was obtained. Solid lines represent the models fitted to both stars, X Ari in the case of the RRab star V1, and a template based on T Sex and DH Peg in the case of the RRC star V2.

BHB star has independent observations from AAT, IMACS, and VLT. The weighted average velocity is $v_{\text{hel}} = 331.7 \pm 2.0 \text{ km s}^{-1}$, showing no evidence of binary motion. For comparison, Muñoz et al. (2006) detect a group of LMC stars in the field of the Carina dwarf spheroidal galaxy ($\sim 22^\circ$ from the LMC center and $\sim 10^\circ$ from Car II and Car III) with an average radial velocity around $v_{\text{hel}} = 332 \text{ km s}^{-1}$. Therefore, the distance and velocity of this BHB star both suggest an association with the LMC. It lies about 18° from the center of the LMC, making it one of the LMC's most distant spectroscopically confirmed BHB members. Clearly, finding additional LMC stars with similar radial velocity at separate positions on the sky would help our understanding of the structure and dynamics of the LMC's outer regions.

3.2.2. RR Lyrae Stars

Car II contains three RR Lyrae stars (Paper I). Our spectroscopic runs targeted two of those stars, namely MAGLITES J073637.00–580114.5 and MAGLITES J073645.86–575154.1 (or V1 and V2 in Paper I), which are the two innermost of the RR Lyrae stars, with projected distances from the center of Car II of 2.1' and 7.7'. The derivation of the center-of-mass velocity, or systemic velocity, of RR Lyrae stars requires special treatment since the radial velocity for these stars changes significantly (up to $\sim 100 \text{ km s}^{-1}$ for RRab stars) during their pulsation cycle. A model of a radial velocity curve must be fitted to the spectroscopic data. To do this, we followed the procedure developed in Vivas et al. (2008). The observational data and the fitted model for each star are shown in Figure 3. As the period of RR Lyrae stars is usually less than a day, we measured the

velocities from the January 23 and 25 AAT observations separately. For other measurements, we used the velocity measured over one to three combined exposures from that night, as reported in Table 4. We therefore have five independent velocity measurements for V1 and three for V2.

For V1, an RRab star, we used the radial velocity model of the star X Arietis, which was parameterized by Layden (1994) based on observations made by Oke (1966). The radial velocity curve of the ab-type RR Lyrae stars (the type of our star V1) has a large discontinuity near maximum light. Thus, it is advisable not to measure radial velocities near that phase in the pulsation cycle ($\phi < 0.05$ or $\phi > 0.9$). However, at the time of the spectroscopic observations we had not obtained final light curves of the RR Lyrae stars, and thus spectra were taken at random phases. Phases were calculated later once the light curves were characterized by Paper I. One of our observations for V1 was indeed not useful since the spectrum was acquired at phase $\phi = 0.93$. Thus, the radial velocity curve was fitted using four observations with phases ranging from 0.08 to 0.58. As seen in Figure 3, all the individual observations follow very nicely the model of X Arietis, which was shifted in velocity to match the observations. The best match was produced when the systemic velocity was 491 km s^{-1} . The rms of the fit is 2.8 km s^{-1} . However, to obtain a more realistic error we followed Vivas et al. (2005) and included uncertainties due to star-to-star variations of the amplitude of the radial velocity curve as well as possible differences on the exact phase of the systemic velocity. We determined a final systemic (heliocentric) velocity for V1 of $491 \pm 7 \text{ km s}^{-1}$.

For V2, which is an RRc star, we used a template constructed by Duffau et al. (2006) based on observations of T Sex and DH Peg. The amplitude of the radial velocity curve of RRc stars is not as large as for RRab variables, nor is there a discontinuity at maximum light. Thus, all three spectra available for this star can be used to determine its velocity. We measured a heliocentric velocity for V2 of $474 \pm 5 \text{ km s}^{-1}$.

The systemic radial velocities obtained for these two RR Lyrae stars confirm that they are members of Car II.

3.3. Velocity Dispersion

We used eight RGB stars (excluding the two binaries mentioned in Section 3.2) and six BHB stars (hereafter the 14 star sample) to calculate the systemic velocity and the velocity dispersion of Car II using the two-parameter Gaussian likelihood function defined in Walker et al. (2006) and an MCMC to sample the distributions of the systemic velocity v_{hel} and the velocity dispersion σ_v . We used a flat prior for the systemic velocity with range (455, 495) km s^{-1} and a non-informative Jeffreys prior for the velocity dispersion with range (0.01, 100) km s^{-1} (or equivalent to a flat prior in $\log(\sigma_v)$ space with range (-2, 2)). The probability distribution from the MCMC is shown in Figure 4. We find a systemic velocity of $v_{\text{hel}} = 477.2 \pm 1.2 \text{ km s}^{-1}$ and a velocity dispersion of $\sigma_v = 3.4^{+1.2}_{-0.8} \text{ km s}^{-1}$, where we report the median of the posterior and the uncertainty calculated from the 16th and 84th percentiles.

In order to test the effects of our input assumptions, we also calculated the systemic velocity and velocity dispersion with different priors and different data sets. A summary of these comparisons is presented in Table 3. With a flat prior for velocity dispersion and the same 14 star sample, the velocity dispersion is $3.8^{+1.3}_{-0.9} \text{ km s}^{-1}$, which is slightly higher than the

value determined using the Jeffreys prior with same data set. This result is similar to what was seen in Kim et al. (2015). If we expand our sample to 16 stars by including the two RR Lyrae stars using the velocities derived in Section 3.2.2, both the systemic velocity and the velocity dispersion are very similar to what we determined with the 14 star sample (default sample). We then run similar calculations with only RGB members and only BHB members. The result with eight RGB members is again very similar to our default sample, suggesting that the results are mostly constrained by the RGB members (which have smaller velocity uncertainties). The six BHB members give a smaller dispersion, but with larger uncertainties so that the results are statistically consistent, mainly due to the large velocity uncertainties ($\delta_v \gtrsim 4 \text{ km s}^{-1}$) on the BHB stars.

We also calculated the systemic velocity and velocity dispersion using the results from each instrument to see if there is any instrumental bias. We obtained very consistent results using the VLT data or IMACS data alone, while the AAT data show much smaller dispersion as the members found by AAT are mostly BHBs (plus RR Lyraes and binaries). We additionally calculated the velocity dispersion using the velocity measurements from only one epoch. We included the 14 stars in addition to the two binaries. For each star the measurement with highest S/N was chosen. The derived velocity dispersion was more than doubled compared to that derived from the 14 star sample. This exercise mimics a case in which only single-epoch velocity measurements are made for each star and therefore no binary information is available. Because of the large velocity amplitudes of the two binary stars, observations made near the velocity extrema of the binary orbits can substantially inflate the apparent velocity dispersion of Car II.

Finally, we performed a jackknife test (MacQueen 1967) to assess the robustness of the measured velocity dispersion with the 14 star sample, in particular, to check whether the results are driven by any single star. We removed one star out of the 14 star sample and recomputed the average velocity and velocity dispersion. In the jackknife runs, the average velocity had a median difference of 0.0 km s^{-1} , a standard deviation of 0.3 km s^{-1} , and a minimum and maximum difference of -0.5 and 0.6 km s^{-1} . For the velocity dispersion the median difference was 0.1 km s^{-1} , the standard deviation 0.2 km s^{-1} , and the minimum and maximum -0.5 and 0.3 km s^{-1} . We conclude that, apart from the binaries, there are no individual stars whose inclusion or exclusion from the sample significantly affects the kinematics of Car II.

We checked if Car II contains a velocity gradient following the method in Li et al. (2017). We calculated a best-fit velocity gradient of $0.0 \pm 0.3 \text{ km s}^{-1} \text{ arcmin}^{-1}$, consistent with the null model. We computed the Bayes factor comparing the velocity gradient and constant velocity dispersion models and found $\ln B = -2.2$, which favors the constant velocity dispersion model (we follow Wheeler et al. 2017 to interpret the Bayes' factor value). We conclude that there is no evidence for a velocity gradient in Car II.

For Car III, we determined a systemic velocity of $284.6^{+3.4}_{-3.1} \text{ km s}^{-1}$ and velocity dispersion of $5.6^{+4.3}_{-2.1} \text{ km s}^{-1}$ using the four identified members. We caution that the small number of stars may not lead to a reliable estimate for the velocity dispersion of Car III. Furthermore, a single binary star can easily inflate the velocity dispersion. We give a more

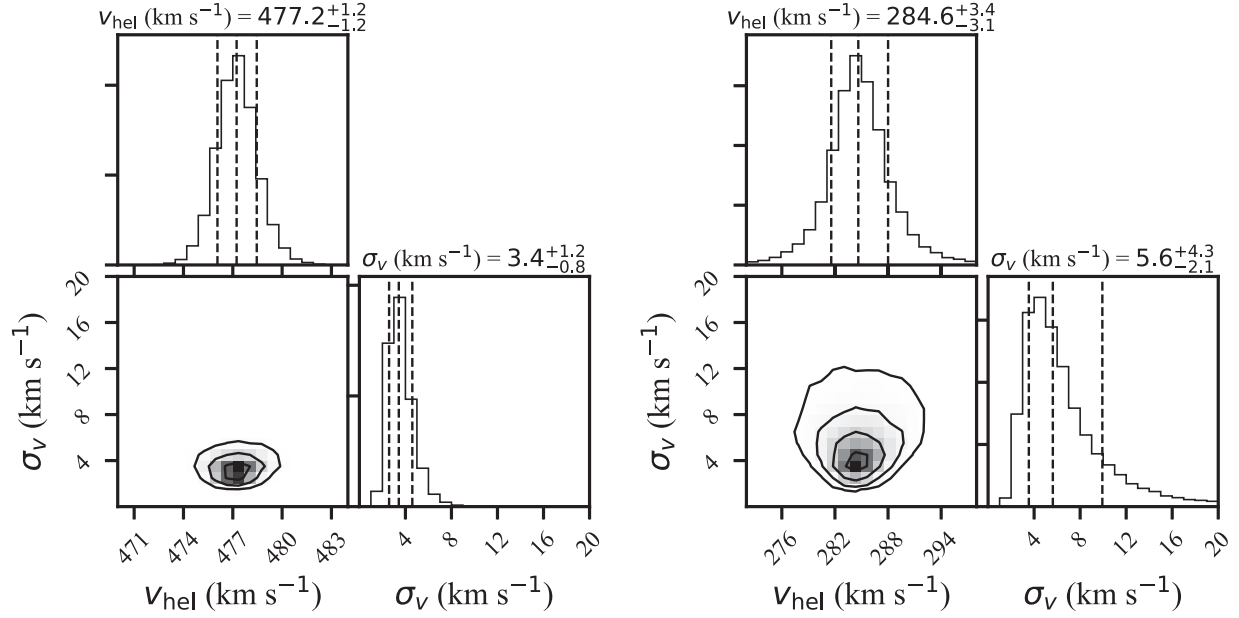


Figure 4. Two-dimensional and marginalized posterior probability distributions from an MCMC sampler using a likelihood model for the systemic velocity and velocity dispersion of Car II (left) and those of Car III (right). The 16th, 50th, and 84th percentiles are indicated by dashed lines in the 1D histograms.

Table 3

Systemic Velocity and Velocity Dispersion with Different Data Sets

Name	Data Set	Prior	v_{hel} (km s ⁻¹)	σ_v (km s ⁻¹)
14 star sample (default)	8 RGB + 6 BHB	Jeffreys	477.2 ± 1.2	$3.4^{+1.2}_{-0.8}$
14 star sample	8 RGB + 6 BHB	flat	477.2 ± 1.3	$3.8^{+1.3}_{-0.9}$
16 star sample	8 RGB + 6 BHB + 2 RRL	Jeffreys	477.4 ± 1.2	$3.5^{+1.2}_{-0.9}$
RGB only	8 RGB	Jeffreys	476.6 ± 1.2	$3.5^{+1.3}_{-0.9}$
BHB only	6 BHB	Jeffreys	478.8 ± 2.2	$0.9^{+3.7}_{-0.9}$
IMACS only	4 RGB	Jeffreys	475.8 ± 2.1	$4.0^{+2.7}_{-1.7}$
VLT only	4 RGB + 2 BHB	Jeffreys	477.1 ± 1.5	$3.3^{+1.7}_{-1.1}$
AAT only	5 BHB	Jeffreys	480.9 ± 2.5	$0.2^{+2.4}_{-0.2}$
one-epoch	10 RGB (incl. 2 Binary) + 6 BHB	Jeffreys	477.8 ± 2.2	$7.7^{+1.8}_{-1.4}$

Note. All values reported here (and in this paper) are from the 50th percentile of the posterior probability distributions. The uncertainties are from the 16th and 84th percentiles of the posterior probability distributions.

detailed discussion of the implications of the measurements and the nature of Car III in Section 4.1.

3.4. Metallicity and Metallicity Dispersion

We measured the metallicity of the red giant member stars in both systems using the equivalent widths (EWs) of the CaT lines. Following the procedure described by Simon et al. (2015) and Li et al. (2017), we fitted all three of the CaT lines with a Gaussian plus Lorentzian function and then converted the summed EWs of the three CaT lines to metallicity using the calibration relation from Carrera et al. (2013) with absolute

V magnitude. We first performed the color-transformation from DES- g and DES- r to apparent V magnitude using Equation (5) in Bechtol et al. (2015) and then adopted distance moduli of $(m - M) = 17.86$ for Car II members and $(m - M) = 17.22$ for Car III members to calculate absolute magnitudes. The statistical uncertainties on the EWs were calculated from the Gaussian and Lorentzian fit. We added a systematic uncertainty of 0.2 Å (as determined in Li et al. 2017) in quadrature with the statistical uncertainties to obtain the final EW uncertainties. The metallicity uncertainties shown in Table 4 are dominated by the uncertainties on the CaT EWs, with small contributions from the uncertainties on the heliocentric distances, the stellar photometry, and the uncertainties on the calibration parameters from Carrera et al. (2013).

Among the 10 confirmed spectroscopic RGB members in Car II, we successfully measured metallicities for nine stars. The metallicities of the Car II members range from $[\text{Fe}/\text{H}] = -2.7$ to $[\text{Fe}/\text{H}] = -1.9$. We used a Gaussian likelihood model as described above for the velocities to calculate the mean metallicity and metallicity dispersion of Car II. We found a mean metallicity of $[\text{Fe}/\text{H}] = -2.44 \pm 0.09$, with a dispersion of $\sigma_{[\text{Fe}/\text{H}]} = 0.22^{+0.10}_{-0.07}$. The probability distribution from the MCMC is shown in Figure 5.

For Car III, we measured the metallicity of the brightest RGB member, MAGLITES J073834.94–575705.4, and obtained $[\text{Fe}/\text{H}] = -1.97 \pm 0.12$ for this star. If this RGB member represents the mean metallicity of Car III, then the metallicities of Car II and Car III are different at 3- σ level. Note that in Paper I we obtained $[\text{Fe}/\text{H}] = -1.8 \pm 0.1$ for Car II and $[\text{Fe}/\text{H}] = -1.8 \pm 0.2$ for Car III from the isochrone fitting using photometry alone. While this metallicity estimate for Car III is consistent with that of the brightest RGB member from the spectroscopic measurements, for Car II the metallicity derived from isochrone fitting is more metal-rich than its spectroscopic mean metallicity.

Table 4
Velocity and Metallicity Measurements

ID	α_{2000} (deg)	δ_{2000} (deg)	g_0^a (mag)	r_0^a (mag)	Masks/ Instruments	MJD	S/N	v (km s ⁻¹)	EW (Å)	[Fe/H]	Comment
Carina II											
MAGLITES J073504.92–575646.9	113.77049	−57.94636	18.18	18.35	AAT–Jan	57777.7	7.9	482.80 ± 3.38	BHB
					AAT–May	57902.4	3.3	487.20 ± 12.63	
MAGLITES J073546.15–574911.6	113.94231	−57.81988	18.68	19.02	AAT–Jan	57777.7	4.4	484.66 ± 6.53	BHB
MAGLITES J073558.28–580328.2	113.99285	−58.05784	19.25	18.81	IMACS–Car2Mask2	57778.3	4.8	475.96 ± 2.47	1.78 ± 0.28	−2.74 ± 0.18	
MAGLITES J073558.39–581227.7	113.99329	−58.20769	18.36	18.61	AAT–Jan	57777.7	4.1	485.43 ± 13.64	BHB
MAGLITES J073559.15–575918.2	113.99644	−57.98838	18.93	18.45	IMACS–Car2Mask2	57778.3	7.3	470.93 ± 1.62	2.45 ± 0.24	−2.43 ± 0.13	
MAGLITES J073601.33–575843.8	114.00552	−57.97885	18.26	17.76	VLT–Feb	57811.1	32.9	472.34 ± 1.03	2.99 ± 0.28	−2.32 ± 0.14	
MAGLITES J073611.87–581228.6	114.04945	−58.20796	18.23	18.46	AAT–Jan	57777.7	6.0	478.94 ± 8.75	BHB
MAGLITES J073621.25–575800.3	114.08852	−57.96675	16.98	16.30	AAT–Jan	57777.7	40.7	492.70 ± 0.51	4.30 ± 0.26	−2.07 ± 0.12	Binary
					IMACS–Car2Mask2	57778.3	42.4	494.30 ± 1.03	4.66 ± 0.22	−1.92 ± 0.10	
					AAT–May	57902.4	20.1	464.92 ± 0.83	4.44 ± 0.32	−2.01 ± 0.14	
MAGLITES J073624.62–575922.1	114.10256	−57.98948	18.89	18.36	IMACS–Car2Mask2	57778.3	7.3	479.46 ± 2.10	
					IMACS–Car2Mask1	57779.3	8.3	481.56 ± 1.90	2.24 ± 0.90	−2.56 ± 0.48	
MAGLITES J073624.98–575714.3	114.10408	−57.95397	18.43	17.97	VLT–Feb	57811.1	31.5	477.75 ± 1.11	2.01 ± 0.20	−2.77 ± 0.12	
MAGLITES J073637.00–580114.5	114.15416	−58.02069	18.56	18.36	AAT–Jan	57777.7	9.0	489.30 ± 1.84	RR Lyrae
					IMACS–Car2Mask2	57778.3	9.3	457.03 ± 2.25	
					IMACS–Car2Mask1	57779.3	8.1	498.71 ± 1.63	
					AAT–May	57902.4	4.6	440.82 ± 14.58	
MAGLITES J073645.86–575154.1	114.19109	−57.86503	17.97	18.02	AAT–Jan	57777.7	8.3	484.83 ± 2.01	RR Lyrae
					IMACS–Car2Mask1	57779.3	10.4	457.63 ± 2.06	
MAGLITES J073646.47–575910.2	114.19362	−57.98617	19.39	18.93	AAT–Jan	57777.7	3.6	485.57 ± 4.42	Binary
					IMACS–Car2Mask2	57778.3	5.4	484.15 ± 3.17	
					IMACS–Car2Mask1	57779.3	5.0	486.62 ± 2.59	2.62 ± 0.29	−2.26 ± 0.15	
					VLT–Feb	57811.1	17.5	460.69 ± 1.37	2.82 ± 0.30	−2.16 ± 0.16	
MAGLITES J073655.60–580049.8	114.23168	−58.01383	18.99	18.52	IMACS–Car2Mask2	57778.3	7.2	475.21 ± 1.92	
MAGLITES J073729.30–580447.8	114.37206	−58.07993	19.14	18.68	VLT–Feb	57811.1	19.6	479.53 ± 1.32	2.42 ± 0.33	−2.40 ± 0.18	
MAGLITES J073737.04–574925.5	114.40434	−57.82375	19.09	19.46	VLT–Feb	57811.1	6.0	481.13 ± 8.25	BHB
MAGLITES J073739.81–580507.0	114.41589	−58.08528	17.80	17.25	VLT–Feb	57811.1	46.8	480.22 ± 0.97	2.52 ± 0.26	−2.64 ± 0.13	
MAGLITES J073745.86–580406.7	114.44108	−58.06853	18.28	18.52	AAT–Jan	57777.7	4.1	467.44 ± 8.43	BHB
					VLT–Feb	57811.1	16.9	474.10 ± 2.80	
Carina III											
MAGLITES J073823.68–575150.8	114.59866	−57.86412	20.21	19.71	VLT–Feb	57811.1	6.4	290.56 ± 4.99	
MAGLITES J073834.84–575211.2	114.64516	−57.86977	17.60	17.77	AAT–Jan	57777.7	8.5	277.14 ± 3.93	BHB
					IMACS–Car3LongSlit	57779.3	6.9	282.26 ± 2.99	
MAGLITES J073834.94–575705.4	114.64558	−57.9515	17.70	17.18	IMACS–Car3Mask1	57778.2	29.9	280.19 ± 1.29	3.73 ± 0.25	−1.97 ± 0.12	
					VLT–Feb	57811.1	43.8	280.36 ± 1.00	3.73 ± 0.28	−1.97 ± 0.13	
MAGLITES J073835.54–575622.3	114.64808	−57.93952	17.53	17.68	IMACS–Car3Mask1	57778.2	15.6	288.25 ± 1.56	BHB
					VLT–Feb	57811.1	23.8	291.92 ± 1.86	
					AAT–May	57902.4	4.4	288.25 ± 4.92	
Non Member ^b											
MAGLITES J073507.41–574725.4	113.78087	−57.79038	18.13	17.89	AAT–Jan	57777.7	13.5	291.13 ± 1.80	3.56 ± 0.56	...	
					AAT–May	57902.4	7.3	298.29 ± 2.30	
MAGLITES J073613.95–580641.2	114.05814	−58.11145	18.31	17.92	AAT–Jan	57777.7	10.0	396.63 ± 1.81	2.64 ± 0.63	...	
					AAT–May	57902.4	6.9	388.58 ± 2.72	
MAGLITES J073629.58–574940.0	114.12327	−57.82777	18.21	17.96	AAT–Jan	57777.7	8.9	309.01 ± 2.19	3.55 ± 0.36	...	
MAGLITES J073634.86–580340.6	114.14526	−58.06127	18.51	18.70	AAT–Jan	57777.7	5.5	329.64 ± 3.85	BHB

Table 4
(Continued)

ID	α_{2000} (deg)	δ_{2000} (deg)	g_0^a (mag)	r_0^a (mag)	Masks/ Instruments	MJD	S/N	v (km s ⁻¹)	EW (Å)	[Fe/H]	Comment
					IMACS-Car2Mask2	57778.3	4.0	327.09 ± 3.91	
					VLT-Feb	57811.1	14.4	335.29 ± 2.87	
MAGLITES J073651.54–580247.8	114.21475	–58.04662	18.07	17.79	IMACS-Car2Mask2	57778.3	11.8	294.38 ± 1.41	4.29 ± 0.39	...	
MAGLITES J073710.30–575819.3	114.29293	–57.97202	19.92	19.55	VLT-Feb	57811.1	9.5	261.93 ± 3.18	4.20 ± 0.59	...	
MAGLITES J073727.87–574421.9	114.36613	–57.73943	18.21	17.93	AAT-Jan	57777.7	11.3	266.26 ± 1.66	5.17 ± 0.44	...	
					AAT-May	57902.4	5.2	294.10 ± 4.91	

Notes.

^a (a) Quoted magnitudes represent the weighted-average point-spread function magnitude derived from the original MagLiteS survey (rather than the photometry from time-series follow-up observations that were used to search for RR Lyrae stars). The photometry provided here is the dereddened photometry using the extinction map from Schlegel et al. (1998). At the location of Car II and Car III, the average color excess is $E(B - V) \sim 0.19$.

^b For non-members, only stars with $v_{\text{hel}} > 220$ km s⁻¹ are presented here. The remaining non-members are available in the online version in machine readable format.

(This table is available in its entirety in machine-readable form.)

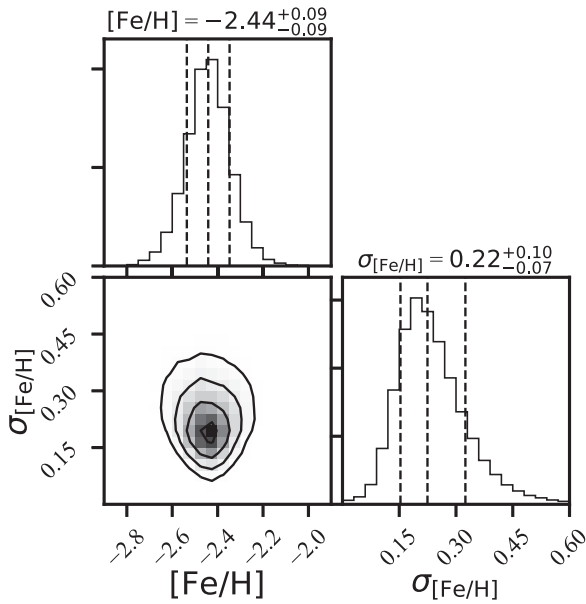


Figure 5. Two-dimensional and marginalized posterior probability distributions from an MCMC sampler using a likelihood model for the mean metallicity and metallicity dispersion of Car II. The 16th, 50th, and 84th percentiles are indicated by dashed lines in the one-dimensional histograms.

4. Discussion

4.1. Properties of Car II and Car III and their Possible Association

We calculated the mass of Car II contained within the half-light radius according to the mass estimator from Wolf et al. (2010) (see also Walker et al. 2009b), using the velocity dispersion determined in Section 3.3 and the half-light radius of Car II from Paper I. We found a dynamical mass of $M_{1/2} = 1.0^{+0.8}_{-0.4} \times 10^6 M_{\odot}$ and a mass-to-light ratio of $369^{+309}_{-161} M_{\odot}/L_{\odot}$ for Car II. The reported uncertainties on the dynamical mass and mass-to-light ratio include the uncertainties on the velocity dispersion from this paper, and the uncertainties on the half-light radius and luminosity from Paper I. The mass of Car II is much larger than its stellar mass, and the mass-to-light ratio is similar to those of other dwarf galaxies with comparable luminosities. The low average metallicity (-2.44 ± 0.09) and large metallicity dispersion ($0.22^{+0.10}_{-0.07}$) also match observations of other dwarf galaxies with similar luminosities (Kirby et al. 2013). We therefore conclude that Car II is a dark-matter-dominated dwarf galaxy.

Because we have only identified four members of Car III, neither its mass nor its metallicity distribution is significantly constrained. We therefore cannot determine whether Car III is a dwarf galaxy. If the metallicity of the brightest confirmed member star ($[\text{Fe}/\text{H}] = -1.97$) represents the average metallicity of the system, then Car III is more metal-rich than most of the dwarf galaxies with similar luminosities, but still much more metal-poor than all known star clusters at a similar luminosity. If the velocity dispersion calculated from the four confirmed members is close to the true dispersion of the system, then Car III is likely to be a dark-matter-dominated dwarf galaxy. Given the small sample, though, a single binary star could easily inflate the velocity dispersion, and therefore

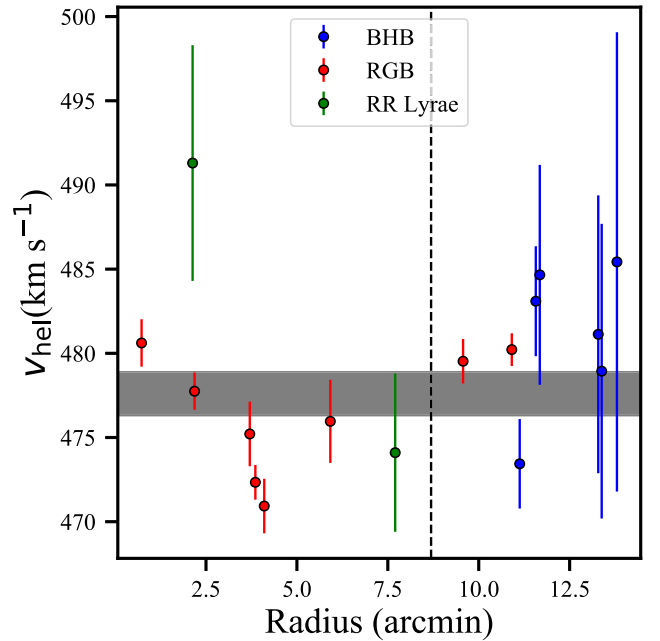


Figure 6. Velocity as a function of distance to the center of Car II, for Car II members only. Two binary stars are not shown. For the two RR Lyrae stars, the systemic velocities calculated in Section 3.2.2 are used. The six outermost member stars are BHB members at $r > 10'$. The shaded region shows the systemic velocity of Car II with $1\text{-}\sigma$ uncertainty. The dashed line shows the half-light radius of Car II from Paper I.

this dispersion shall be used with caution. Interestingly, among the four member stars, MAGLITES J073834.94–575705.4, the brightest RGB member, was observed in both January (IMACS) and February (VLT), and MAGLITES J073835.54–575622.3, a BHB member, was observed in January (IMACS), February (VLT), and May (AAT). The differences in velocities are consistent with the measurement uncertainties (see Table 4) and therefore we do not see any strong evidence for binarity of these two stars from our observations across 1–3 month baselines. However, the velocities of these two stars are about 8 km s^{-1} apart (and are the source of the large velocity dispersion on Car III). This large difference, if indeed not caused by binary motion, could provide a hint that Car III should be classified as a dwarf galaxy. Identifying more members with deeper observations will be necessary to confirm the nature of Car III. Observing these bright members at one or two additional epochs will also help determine whether or not they are in binary systems.

We note that the mass estimator from Wolf et al. (2010) is only valid for dispersion-supported stellar systems in dynamical equilibrium. It is possible that Car II has had a tidal interaction with the Milky Way ($d \sim 36 \text{ kpc}$), LMC ($d \sim 20 \text{ kpc}$), or Car III ($d \sim 10 \text{ kpc}$) due to their close proximity. Either a velocity gradient or an increasing velocity dispersion at large radii could be potential signs of tidal disruption. In Section 3.3, we conclude that we are not able to detect a velocity gradient with our current data. In Figure 6, we show the velocity as a function of distance to the center of Car II. Interestingly, the six BHB stars are also the outermost members. As shown in Table 3, the velocity dispersion from the BHB sample alone is small due to the large velocity uncertainties and, therefore, we

also do not see a larger velocity dispersion at large radii. However, we note that both null results could result from the large velocity uncertainties of these BHB stars. Further studies that either identify more RGB stars at large radii or improve the velocity precision for the known BHB members will be necessary to completely rule out a velocity gradient or other tidal effects.

The fact that all six BHB members are the outermost stars (Figure 6) implies a possible non-uniform spatial distribution of the stellar populations in Car II. However, we also caution that this distribution is likely caused by a selection bias from the observations. Note that the four outermost BHB members are uniquely identified by AAT, which has the largest FOV among three instruments. However, the target selection for AAT was performed with an older version of PARSEC isochrones and therefore may have missed a few RGB members with $r > r_h$, as explained in the Appendix. Further observations, including a more comprehensive search for bright RGB members outside of the half-light radius, may be necessary to fully understand the possible stellar population dependent spatial distribution in Car II.

To check whether the observed kinematics of Car II and Car III are consistent with their being gravitationally bound systems, we have computed their tidal radii (r_t) with the Milky Way as the host via Equation (18) in Bonnavard et al. (2015a), using the Milky Way mass model presented in Eadie & Harris (2016). To set a lower limit on r_t , we used the Car II $M_{1/2}$ value for the total mass and found $r_t \sim 500$ pc. This lower limit on r_t is already significantly larger than the observed size of the system. With a mass profile based on a Navarro et al. (1996) profile, the total mass of Car II (with $r = 300$ pc) is estimated to be 5–10 times larger than $M_{1/2}$ (with $r_s = 0.1$ –0.5 kpc), implying $r_t \sim 0.9$ –1.1 kpc. The mass profile of Car III is more uncertain due to the small number of stars and the unknown nature of the object. If we assume conservatively that Car III is a dwarf galaxy with dispersion $\sigma = 1$ km s⁻¹ and $M(r_{\max}) = 10 \times M_{1/2}$, then we find $r_t \sim 250$ pc, again much larger than the observed size of Car III. If the true dispersion of Car III is close to the measurement from a sample of four members, then the tidal radius will be even larger. We additionally computed r_t assuming that the LMC is the host instead of the Milky Way. For Car II, the LMC host r_t values are 5%–10% larger than the Milky Way host values while for Car III they are $\sim 50\%$ larger. Although a complete analysis of the Car II tidal radius should include the LMC+Milky Way system, we still expect the tidal radius to be larger than the observed size of Car II. Therefore, we conclude that Car II is likely to be a bound system based on its current location in the Milky Way, though it is still possible that it had a smaller tidal radius if it approached closer to the Milky Way or LMC in the past.

The small projected separation ($\sim 18'$) of Car II and Car III and their similar distances naturally lead to the question of whether the two are (or were) a bound pair of satellites. Similar speculation has occurred for the satellite pairs Leo IV–Leo V ($\Delta d_{3D} \sim 20.6$ kpc and $\Delta v \sim 47$ km s⁻¹; Belokurov et al. 2008; Walker et al. 2009a; de Jong et al. 2010) and Pisces II–Pegasus III ($\Delta d_{3D} \sim 43$ kpc and $\Delta v \sim 10$ km s⁻¹; Kim et al. 2015, 2016). While Car II and Car III have the smallest known physical separation to date, $\Delta d_{3D} \sim 10$ kpc, their separation in velocity is quite large $\Delta v \sim 193$ km s⁻¹.

We applied the method presented in Evslin (2014) to estimate the minimum halo mass for the Car II–Car III system to be bound and found an unrealistically large halo mass of $\sim 10^{11} M_\odot$ (similar to the halo mass of the LMC; van der Marel & Kallivayalil 2014). Based on the observed kinematics of Car II, the escape velocity at the distance of Car III is between 15 and 25 km s⁻¹, significantly smaller than the observed velocity difference. Car II and Car III are therefore highly unlikely to be a bound pair of satellites.

Assuming the pair have similar proper motions, the two satellites would have had a close encounter and sailed past one another ~ 53 Myr ago. Based on this trajectory and the observed separation they would have passed within 200 pc of one another ($\sim 2 \times (r_{1/2, \text{Car II}} + r_{1/2, \text{Car III}})$). At the point of closest encounter, the Car III tidal radius would have been no more than a few tens of parsecs. Regardless of the nature of Car III, a close encounter between the satellites could have disrupted Car III. While there is no reason to expect Car II and Car III to have similar proper motions given the large difference in their radial velocities, it will be interesting to explore this scenario further when proper motions are available. We note that the brightest spectroscopic members in both Car II and Car III are brighter than the faint limit for *Gaia* proper motion measurements.

The properties of Car II and Car III derived in this paper are summarized in Table 2.

4.2. Association with the Magellanic Clouds

As discussed in Section 1, the MagLiteS survey was designed to search for satellites of the Magellanic Clouds. Having searched in the vicinity of the LMC and SMC, it is therefore unsurprising that Car II and Car III are physically close to the Magellanic Clouds. The newly measured velocities of the Carina pair can now be used to test whether a physical association with the Clouds is likely.

To aid comparison with models, we first transform the line-of-sight velocities of Car II and Car III from the heliocentric frame to the Galactic Standard of Rest frame³⁷ and obtain $v_{\text{GSR, Car II}} = 235$ km s⁻¹ and $v_{\text{GSR, Car III}} = 42$ km s⁻¹. Next, we compare these measurements with the dynamical model of Magellanic satellites presented in Jethwa et al. (2016). Assuming an association with the LMC, this model predicts a velocity of $v_{\text{GSR}} = 118^{+142}_{-80}$ (149⁺¹⁴²₋₁₁₄ km s⁻¹) at the position of Car II (Car III). For an association with the SMC, the predicted velocities are higher, at $v_{\text{GSR}} = 350^{+50}_{-70}$ km s⁻¹ for both Car II and Car III. According to this model, both Carinas therefore have velocities consistent with an LMC association. In Figure 7, we show the comparison between the observed phase-space distribution of dwarf galaxies/dwarf galaxy candidates and the simulated probability distribution of LMC satellites from the Jethwa et al. (2016) model, and the neutral hydrogen gas column density from Nidever et al. (2010). According to the Jethwa et al. model, both Car II and Car III are consistent with having originated with the LMC.

As pointed out in Section 3.2.1, the non-rotating LMC halo population and the LMC rotating disk both have $v_{\text{hel}} \sim 380$ km s⁻¹ at the location of Car II and Car III, which differs

³⁷ We adopted the circular orbital velocity of Milky Way at the Sun's radius $\Theta_0 = 239$ km s⁻¹ (McMillan 2011) and solar motion of $(U_\odot, V_\odot, W_\odot) = (11.1, 12.24, 7.25)$ km s⁻¹ (Schönrich et al. 2010) for the velocity transformation from heliocentric to Galactic Standard of Rest to match the values used in Jethwa et al. (2016).

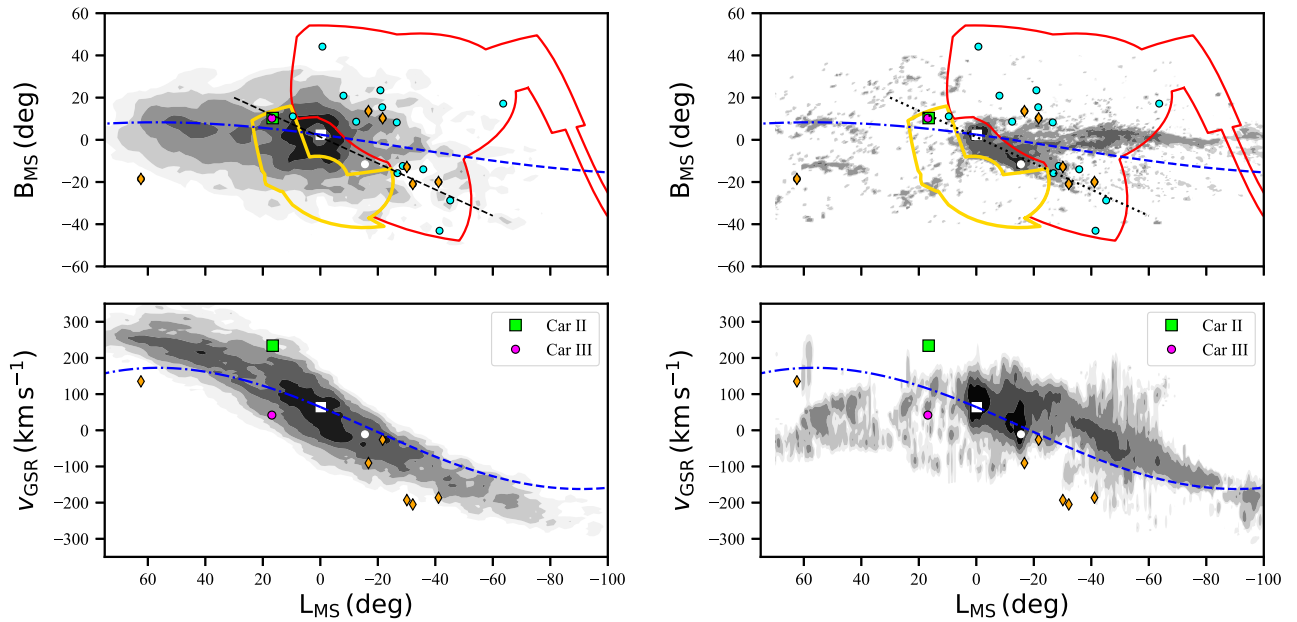


Figure 7. Upper panels: on-sky positions of the newly discovered satellites in DES (red outline) and MagLiteS (yellow outline), together with the LMC (white square) and SMC (white circle), shown in Magellanic Stream coordinates (Nidever et al. 2008). Car II and Car III, the Magellanic Clouds, and several other dwarf galaxies form a tight sequence on the sky. The black dashed line is a fit to this sequence as indicated in Paper I. Lower panels: line-of-sight velocities for ultra-faint satellites near the Magellanic Clouds as a function of Magellanic Stream longitude. Objects with velocities from the literature are plotted as orange diamonds (Kirby et al. 2015b; Koposov et al. 2015; Simon et al. 2015, 2017; Walker et al. 2016), while measurements of Car II and Car III from this work are displayed in green and magenta, respectively. The gray contours show the probability distribution of the LMC satellites from Jethwa et al. (2016) (left) and the neutral hydrogen column density from Nidever et al. (2010) (right). The dashed–dotted (dashed) curves show the leading (trailing) orbit of the LMC.

by $\sim 100 \text{ km s}^{-1}$ from the heliocentric velocities of Car II and Car III. According to van der Marel & Kallivayalil (2014), the enclosed LMC mass out to a radius of 8.7 kpc is $M(<8.7 \text{ kpc}) = 1.7 \times 10^{10} M_{\odot}$. The corresponding escape velocity is $\sim 90 \text{ km s}^{-1}$ at the distance of Car II ($\sim 18 \text{ kpc}$ from the LMC) and $\sim 75 \text{ km s}^{-1}$ at the distance of Car III ($\sim 25 \text{ kpc}$ from the LMC). Because these values are based on a lower limit to the enclosed mass of the LMC, the actual escape velocities are likely to be somewhat larger. Therefore, we tentatively suggest that one or both of Car II and Car III are likely to be bound satellites of the LMC, although proper motion measurements will be needed to confirm this hypothesis.

We also note that all three newly discovered MagLiteS satellite candidates (Car II, Car III, and Pictor II) fall along a linear sequence on the sky as defined by the positions of the LMC, SMC, and seven of the DES satellite candidates. This configuration is shown by the dashed black line in Figure 7. This linear sequence was first pointed out in Jethwa et al. (2016), prior to any MagLiteS discoveries. As discussed in Paper I, it is unclear whether this linear sequence corresponds to a planar distribution of satellites around the Magellanic Clouds, or simply a satellite distribution that is elongated along the LMC–SMC separation vector. Once dynamical models of both scenarios are available, the velocities we have measured may provide a useful discriminant.

4.3. J - and D -factors

Milky Way satellite galaxies are among the most promising targets for indirect dark matter searches due to their substantial dark matter content, proximity, and dearth of conventional non-thermal emission (e.g., Baltz et al. 2008; Winter et al. 2016). In

particular, analyses of γ -ray data from the *Fermi* Large Area Telescope (LAT) around previously known Milky Way satellites are now sensitive to dark matter annihilating at the canonical thermal relic cross section for particle masses up to 100 GeV (e.g., Ackermann et al. 2015a; Geringer-Sameth et al. 2015b). The discovery of additional Milky Way satellites, especially nearby objects such as Car II and Car III, can improve the sensitivity of such searches (He et al. 2015; Charles et al. 2016), as demonstrated by Drlica-Wagner et al. (2015a) and Albert et al. (2017).

In this subsection, we compute the astrophysical component of the dark matter annihilation and decay fluxes, the so-called J - and D -factors, for both Car II and Car III. The J -factor is the line-of-sight integral of the dark matter density squared: $J(\theta) = \int \rho_{\text{DM}}^2 d\Omega dl$. The D -factor is the linear analog: $D(\theta) = \int \rho_{\text{DM}} d\Omega dl$. Here, ρ_{DM} is the dark matter density and the integral is performed over a solid angle $\Delta\Omega$ with radius θ . The standard approach for computing ρ_{DM} in dwarf spheroidal galaxies uses the spherical Jeans equation (e.g., Strigari et al. 2008; Bonnavard et al. 2015b).

The three main ingredients of a spherical Jeans analysis are: the stellar density profile, which we modeled as a Plummer profile (Plummer 1911); the gravitational potential, assumed to be dark matter dominated and modeled with a Navarro–Frenk–White profile (Navarro et al. 1996); and the stellar anisotropy, modeled with a constant profile.³⁸ Jeffreys priors are assumed for the dark matter halo parameters: $-2 < \log_{10}(r_s/\text{kpc}) < 1$ and $4 < \log_{10}(\rho_s/M_{\odot} \text{ kpc}^{-3}) < 14$ for the scale radius, r_s , and scale density, ρ_s , respectively. Additionally, a prior of $r_s > r_{1/2}$ is

³⁸ Analysis with generalized stellar, dark matter, and anisotropy profiles would produce larger confidence intervals (Bonnivard et al. 2015a).

imposed, where $r_{1/2}$ is the azimuthally averaged stellar half-light radius. We adopted the $r_s > r_{1/2}$ prior for several reasons: in our posterior distributions there are no trends between J and r_s except for $r_s < r_{1/2}$ where J is systematically higher, the J -factor tends to be overestimated in mock data sets without this cut (see Section 4.1 of Bonnavard et al. 2015b), and small r_s values are disfavored in Λ CDM N -body simulations (based on Garrison-Kimmel et al. 2014, a halo with $V_{\max} \sim 5\text{--}10 \text{ km s}^{-1}$ has a $r_s \sim 100\text{--}300 \text{ pc}$). For the anisotropy prior, we assumed a flat symmetrized anisotropy parameter; $-0.95 < \tilde{\beta} < 1.0$ (see Equation (8) in Read et al. 2006). A flat prior was used for the average velocity ($470 < \bar{v} < 490 \text{ km s}^{-1}$) and Gaussian priors were assumed for the distance and structural parameters.³⁹ We used an unbinned likelihood function (Strigari et al. 2008; Martinez et al. 2009; Geringer-Sameth et al. 2015a) and determined posterior distributions with the MultiNest sampling routine (Feroz & Hobson 2008; Feroz et al. 2009). We estimated the dark matter r_t (required to compute the J - and D -factors) at each point in the posterior distribution by iteratively computing the enclosed mass and solving for r_t as described in Section 4.1. We find the Car II r_t posterior to be roughly Gaussian, centered at 1 kpc but containing a substantial tail to larger values.

We calculated the Car II integrated J -factor enclosed within solid angles of radii $\theta = \alpha_c, 0.1, 0.2, 0.5$ to be $\log_{10}(J/\text{GeV}^2 \text{ cm}^{-5}) = 18.1^{+0.5}_{-0.5}, 17.9^{+0.6}_{-0.5}, 18.0^{+0.5}_{-0.5}, 18.2^{+0.5}_{-0.5}$, respectively, using the 14 star sample. α_c is the angle within which the J -factor errors are minimized (Walker et al. 2011); $\alpha_c = 2r_{1/2}/d \approx 0.23$ for Car II. The equivalent radius for the D -factor occurs at $\alpha_c/2$. We determined the D -factor within $\theta = \alpha_c/2, 0.1, 0.2, 0.5$ to be $\log_{10}(D/\text{GeV} \text{ cm}^{-2}) = 17.1^{+0.3}_{-0.3}, 16.9^{+0.3}_{-0.3}, 17.4^{+0.3}_{-0.3}, 18.0^{+0.4}_{-0.4}$. These values agree with the simple J -factor estimator (Equation (13) of Evans et al. 2016). This value is an order of magnitude smaller than the simple empirical J -distance scaling relations (Drlica-Wagner et al. 2015a; Albert et al. 2017). The J -factor contains a large velocity dispersion scaling ($J \propto M^2 \propto \sigma^4$) and an increase of only $\Delta\sigma \sim 1.5 \text{ km s}^{-1}$ would move Car II onto the J -distance scaling relation (Pace & Strigari 2018). There are multiple ultra-faint satellites with larger J -factors (6–8 are larger depending on the J -factor compilation; Bonnavard et al. 2015a; Geringer-Sameth et al. 2015a). The D -factor at 0.1 is smaller than most of the other dwarf spheroidals (Bonnivard et al. 2015a). Though Car II has similar heliocentric distance and velocity dispersion to Ret II, its J -factor is smaller because it has a larger $r_{1/2}$ (Pace & Strigari 2018). Car II is therefore not the most promising individual target for a dark matter annihilation signal but will be a useful addition in stacked analyses.

We applied the same methodology to the four star sample of Car III. We find the integrated J -factor within solid angles of radii $\theta = \alpha_c, 0.1, 0.2, 0.5$ to be $\log_{10}(J/\text{GeV}^2 \text{ cm}^{-5}) = 19.8^{+1.0}_{-0.9}, 19.9^{+1.0}_{-0.9}, 20.1^{+1.0}_{-0.9}, 20.2^{+1.0}_{-0.9}$, respectively. $\alpha_c = 0.08$ for Car III. The D -factor for Car III within $\theta = \alpha_c/2, 0.1, 0.2, 0.5$ is $\log_{10}(D/\text{GeV} \text{ cm}^{-2}) = 17.2^{+0.5}_{-0.4}, 17.8^{+0.5}_{-0.5}, 18.3^{+0.6}_{-0.5}, 18.8^{+0.6}_{-0.7}$. The J -factor estimation of Car III is larger than that of Car II due to its proximity, smaller size, and larger (but uncertain) velocity dispersion. From our analysis, Car III

potentially has one of the largest J -factors. However, given the very small stellar kinematic sample and the uncertain classification of Car III, it is premature to draw strong conclusions about the suitability of Car III as a dark matter annihilation target. As discussed in Section 4.1, the large velocity dispersion could result from binary star motions, small number statistics, or possible tidal effects. As a cautionary case in point, the Triangulum II ultra-faint dwarf galaxy has recently had its J -factor values revised downward due to the identification of previously unsolved binary stars (Genina & Fairbairn 2016; Kirby et al. 2017). In addition, the velocity dispersion of Boötes II has likely been overestimated in past determinations due to the presence of one binary star (Koch et al. 2009; Ji et al. 2016).

4.4. Gamma-ray Observations

We searched for excess γ -ray emission coincident with Car II and Car III using eight years of LAT data (2008 August 4 to 2016 August 5) passing the P8R2_SOURCE event class selection from 500 MeV to 500 GeV. The low-energy bound of 500 MeV was selected to mitigate the impact of leakage from the bright limb of the Earth because the LAT point-spread function broadens considerably below that energy. The high-energy bound of 500 GeV is chosen to mitigate the effect of the increasing residual charged-particle background at higher energies (Ackermann et al. 2015b). To remove γ -rays produced by cosmic-ray interactions in the Earth's limb, we rejected events with zenith angles greater than 100° . To analyze data coincident with Car II and Car III, we used $10^\circ \times 10^\circ$ regions of interest (ROIs) centered on each object. Data reduction was performed using *ScienceTools* version 11-05-03.⁴⁰

We used the maximum-likelihood analysis pipeline described by Ackermann et al. (2014) to test for γ -ray emission coincident with Car II and III in excess of the known astrophysical backgrounds. The background model for the ROI includes Galactic interstellar emission (Acero et al. 2016), isotropic emission,⁴¹ and point sources from a catalog derived from four years of data (3FGL; Acero et al. 2015). Car II and Car III reside in a region of the sky where the diffuse γ -ray background is relatively smooth (Galactic latitude of $\sim 15^\circ$), and the nearest 3FGL catalog source is $\sim 2^\circ$ away.

We first created a detection significance map for the entire $10^\circ \times 10^\circ$ ROI by rastering a putative point source with fixed power-law spectrum ($dN/dE \sim E^{-2}$) across the ROI in 0.1 steps and computing the improvement in the delta log-likelihood test statistic (TS; Mattox et al. 1996). This procedure led to the identification of three additional point-like source candidates in the region, none of which is within 3° of Car II or III (Figure 8). The TS values obtained at the locations of Car II and Car III are 0.16 and 4.2, respectively, both consistent with the background-only hypothesis. We note that Car II and Car III would not be resolvable as independent sources given the resolution of the LAT instrument, which is $\sim 1^\circ$ at 1 GeV and asymptotes to ~ 0.1 above 10 GeV. The TSs associated with Car II and Car III are thus correlated, and can be attributed to a single excess of counts located ~ 0.7 from Car III at $(\alpha, \delta) = (114.5, -57.9)$.

³⁹ We used the azimuthally averaged half-light radius to account for the axisymmetry of the systems ($r_{1/2} = r_{\text{azimuthal}} = r_{\text{major}} \sqrt{1 - \epsilon}$). For non-spherical analysis of dwarf galaxy J -factors see Hayashi et al. (2016) and Sanders et al. (2016).

⁴⁰ <http://fermi.gsfc.nasa.gov/ssc/data/analysis/software/>

⁴¹ <http://fermi.gsfc.nasa.gov/ssc/data/access/lat/BackgroundModels.html>

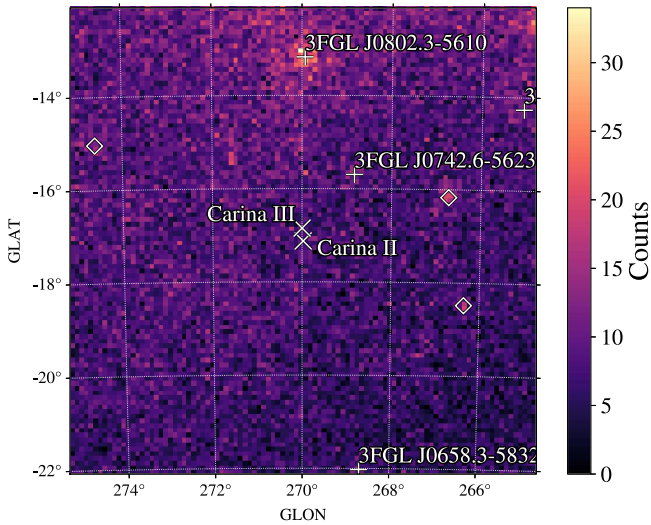


Figure 8. *Fermi*-LAT γ -ray counts map ($E > 1$ GeV) in the vicinity of Car II and Car III (Galactic coordinates). White plus signs indicate the positions of known γ -ray sources from the 3FGL. Open diamonds indicate the positions of new γ -ray point-source candidates found in this analysis.

To search for γ -ray emission consistent with the annihilation of a dark matter particle into standard model products, we fit the γ -ray data coincident with Car II and Car III using a variety of spectral models generated by DMFit (Jeltema & Profumo 2008; Ackermann et al. 2014). We scan a range of dark matter masses spanning from 2 GeV to 10 TeV and annihilating through the $b\bar{b}$ and $\tau^+\tau^-$ channels. The most significant excess has $TS = 6.2$ and occurs for a dark matter particle with mass 35.4 GeV annihilating through the $\tau^+\tau^-$ channel. Given that the statistical significance of this excess is well below the typical point-source detection criteria of the LAT ($TS = 25$), we calculate limits on the dark matter annihilation cross section, $\langle\sigma v\rangle$, using the J -factors derived in Section 4.3. We find that Car II (Car III) can be used to constrain $\langle\sigma v\rangle < 2.2 \times 10^{-24} \text{ cm}^3 \text{ s}^{-1}$ ($3.3 \times 10^{-25} \text{ cm}^3 \text{ s}^{-1}$) for 100 GeV dark matter particles annihilating through the $b\bar{b}$ channel. These constraints are ~ 100 (~ 10) times larger than the thermal-relic cross section (i.e., Steigman et al. 2012). We again caution against overinterpreting the constraints derived from Car III because the J -factor value of Car III is derived from a very small stellar kinematic sample.

5. Summary

In this paper, we presented the first spectroscopic analysis of the Carina II and Carina III dwarf galaxy candidates recently discovered in MagLiteS. Based on the kinematic and chemical properties of 18 confirmed spectroscopic member stars in Car II, we conclude that it is a dark-matter-dominated dwarf galaxy. On the other hand, only four members were identified in Car III. With this small spectroscopic sample we cannot yet determine whether Car III is a compact dwarf galaxy or an extended star cluster.

While Car II and Car III are located very close to each other both in sky projection ($\sim 18'$) and in three dimensions (~ 10 kpc), their systemic velocities differ by $\sim 200 \text{ km s}^{-1}$.

We therefore conclude that these two systems are unlikely to be a pair of bound satellites.

Both Car II and Car III have line-of-sight velocities consistent with the hypothesis that they formed as members of a group of satellites around the LMC. Furthermore, one or both systems might remain bound to the LMC due to the small difference in the line-of-sight velocity. The brightest RGB members in Car II and Car III are bright enough to have proper motion measurements from *Gaia* to test this hypothesis.

We further identify one BHB star as a likely LMC member in the region of Car II. Located at about 18° from the center of the LMC, this star is one of the LMC's most distant spectroscopically confirmed BHB members, and might provide hints on our understanding of the structure and dynamics of the LMC's outer regions.

No statistically significant excess of γ -ray emission is found at the locations of Car II and Car III in eight years of *Fermi*-LAT data. Using the J -factors derived from the kinematics data, Car II and Car III can be used to constrain the dark matter annihilation cross section.

T.S.L. thanks Leo Girardi for helpful discussions regarding the PARSEC isochrones. The authors thank Louis Strigari for helpful conversations regarding the J -factor calculation. The authors thank the anonymous referee for useful comments. We are grateful for the service observations and Director's Discretionary time on the AAT and VLT. We thank the service observers, Jeffrey Simpson and Chris Lidman, for collecting the AAT data during the service runs. We acknowledge the traditional owners of the land on which the AAT stands, the Gamilaraay people, and pay our respects to elders past and present.

This project is partially supported by the NASA *Fermi* Guest Investigator Program Cycle 9 No. 91201. J.D.S. acknowledges support from the National Science Foundation under grant AST-1714873. A.B.P. acknowledges generous support from the George P. and Cynthia Woods Institute for Fundamental Physics and Astronomy at Texas A&M University. M.A.S.C. is supported by the *Atracción de Talento* contract no. 2016-T1/TIC-1542 granted by the Comunidad de Madrid in Spain. A.P.J. is supported by NASA through Hubble Fellowship grant HST-HF2-51393.001 awarded by the Space Telescope Science Institute, which is operated by the Association of Universities for Research in Astronomy, Inc., for NASA, under contract NAS5-26555. B.C.C. acknowledges the support of the Australian Research Council through Discovery project DP150100862. D.M.D. acknowledges support by Sonderforschungsbereich (SFB) 881 “The Milky Way System” of the German Research Foundation (DFG) through sub-projects A2.

This research has made use of NASA's Astrophysics Data System Bibliographic Services. This research made use of *Astropy*, a community-developed core Python package for Astronomy (Astropy Collaboration et al. 2013). Contour plots were generated using *corner.py* (Foreman-Mackey 2016).

This project used data obtained with the Dark Energy Camera (DECam), which was constructed by the Dark Energy Survey (DES) collaboration. Funding for the DES Projects has

been provided by the U.S. Department of Energy, the U.S. National Science Foundation, the Ministry of Science and Education of Spain, the Science and Technology Facilities Council of the United Kingdom, the Higher Education Funding Council for England, the National Center for Supercomputing Applications at the University of Illinois at Urbana-Champaign, the Kavli Institute of Cosmological Physics at the University of Chicago, the Center for Cosmology and Astro-Particle Physics at the Ohio State University, the Mitchell Institute for Fundamental Physics and Astronomy at Texas A&M University, Financiadora de Estudos e Projetos, Fundação Carlos Chagas Filho de Amparo à Pesquisa do Estado do Rio de Janeiro, Conselho Nacional de Desenvolvimento Científico e Tecnológico and the Ministério da Ciência, Tecnologia e Inovação, the Deutsche Forschungsgemeinschaft, and the Collaborating Institutions in the Dark Energy Survey. The Collaborating Institutions are Argonne National Laboratory, the University of California at Santa Cruz, the University of Cambridge, Centro de Investigaciones Energéticas, Medioambientales y Tecnológicas-Madrid, the University of Chicago, University College London, the DES-Brazil Consortium, the University of Edinburgh, the Eidgenössische Technische Hochschule (ETH) Zürich, Fermi National Accelerator Laboratory, the University of Illinois at Urbana-Champaign, the Institut de Ciències de l'Espai (IEEC/CSIC), the Institut de Física d'Altes Energies, Lawrence Berkeley National Laboratory, the Ludwig-Maximilians Universität München and the associated Excellence Cluster Universe, the University of Michigan, the National Optical Astronomy Observatory, the University of Nottingham, the Ohio State University, the OzDES Membership Consortium the University of Pennsylvania, the University of Portsmouth, SLAC National Accelerator Laboratory, Stanford University, the University of Sussex, and Texas A&M University.

Based on observations at Cerro Tololo Inter-American Observatory, National Optical Astronomy Observatory (NOAO Prop. ID 2016A-0366 and PI Keith Bechtol), which is operated by

the Association of Universities for Research in Astronomy (AURA) under a cooperative agreement with the National Science Foundation.

Facilities: *Magellan/Baade* (IMACS), Very Large Telescope (GIRAFEE+FLAME), Anglo-Australian Telescope (AAO-mega+2dF).

Appendix PARSEC Isochrones

In the course of our spectroscopic follow-up campaign on DES ultra-faint satellites (Simon et al. 2015, 2017; Li et al. 2017), we noticed that the location of the confirmed spectroscopic members in CMDs was shifted with respect to the PARSEC isochrones of a metal-poor stellar population in the DECam system (see e.g., Figure 1 in Simon et al. 2017). In particular, the confirmed RGB members are found to have bluer colors than indicated by PARSEC isochrones. This offset is on the order of $g - r \sim 0.05$ mag and could significantly affect the target selection of the candidate members for spectroscopic follow-up. For the IMACS observations presented in this paper, the target selection used criteria similar to those applied by Simon et al. (2017) and therefore the effect caused by this shift was minimal. However, for AAT observations, targets were selected to be near the PARSEC isochrone and therefore most of the RGB members were missed as a result of this color offset. We therefore manually shifted the isochrone bluer for the target selection of VLT observation, as described in Section 2.3.

This offset was only apparent when comparing confirmed members of ultra-faint dwarf galaxies discovered with DECam to the PARSEC isochrone generated in the DECam system. A similar offset is not observed for the ultra-faint dwarfs discovered in the SDSS. After consultation with the Padova team, we learned that the PARSEC isochrones were computed using the filter

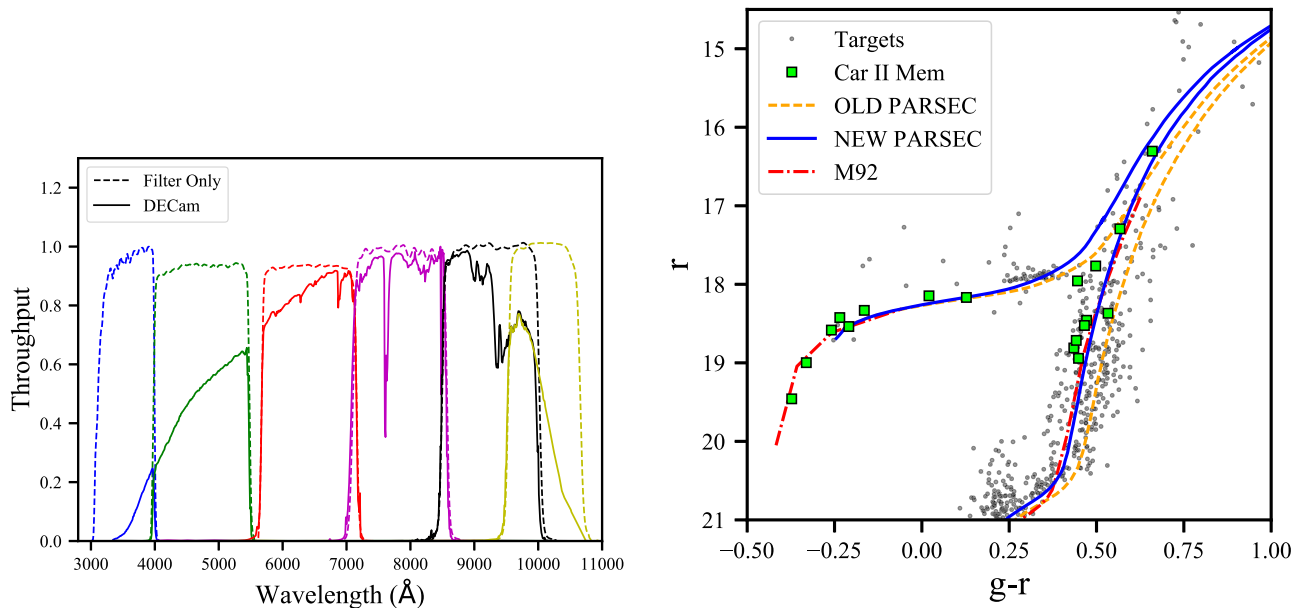


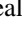
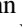

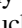




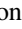
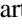
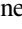



Figure 9. Left: a comparison of the DECam system throughput including filter response only (old) and combined (filter+CCD QE+atmosphere, new), both from the CTIO website. Right: PARSEC isochrones of a metal-poor population with $[\text{Fe}/\text{H}] = -2.2$, age = 12 Gyr using the old and new DECam response. The new isochrone is well aligned with the confirmed members in Car II as well as the empirical isochrone of M92 from An et al. (2008) translated from the SDSS to the DECam system (red dashed lines).

transmission of DECam only. However, in order to compute precise synthetic magnitudes, one should also consider the CCD quantum efficiency (QE), Earth's atmospheric transmission, and the mirror reflectivity, etc. A newer version of the PARSEC models for the DECam system was updated⁴² on 2017 July 17 with the latest version of the system response of DECam.⁴³ A comparison of different versions of DECam throughput and the corresponding PARSEC isochrones is shown in Figure 9. With the corrected DECam system response, the confirmed spectroscopic members in Car II are much closer to the updated PARSEC isochrone. The remaining small offset might be caused by an overestimate of the interstellar extinction.⁴⁴

ORCID iDs

T. S. Li  <https://orcid.org/0000-0002-9110-6163>
 A. B. Pace  <https://orcid.org/0000-0002-6021-8760>
 G. Torrealba  <https://orcid.org/0000-0002-2494-4271>
 K. Kuehn  <https://orcid.org/0000-0003-0120-0808>
 A. Drlica-Wagner  <https://orcid.org/0000-0001-8251-933X>
 A. K. Vivas  <https://orcid.org/0000-0003-4341-6172>
 R. P. van der Marel  <https://orcid.org/0000-0001-7827-7825>
 B. Yanny  <https://orcid.org/0000-0002-9541-2678>
 D. B. Zucker  <https://orcid.org/0000-0003-1124-8477>
 G. Lewis  <https://orcid.org/0000-0003-3081-9319>
 D. L. Nidever  <https://orcid.org/0000-0002-1793-3689>
 M. A. Sánchez-Conde  <https://orcid.org/0000-0002-3849-9164>
 A. P. Ji  <https://orcid.org/0000-0002-4863-8842>
 B. C. Conn  <https://orcid.org/0000-0001-6959-4546>
 N. F. Martin  <https://orcid.org/0000-0002-1349-202X>
 D. Martínez-Delgado  <https://orcid.org/0000-0003-3835-2231>

References

- Abbott, T., Aldering, G., Annis, J., et al. 2005, arXiv:astro-ph/0510346
 Acero, F., Ackermann, M., Ajello, M., et al. 2015, *ApJS*, **218**, 23
 Acero, F., Ackermann, M., Ajello, M., et al. 2016, *ApJS*, **223**, 26
 Ackermann, M., Ajello, M., Albert, A., et al. 2015b, *ApJ*, **799**, 86
 Ackermann, M., Albert, A., Anderson, B., et al. 2015a, *PhRvL*, **115**, 231301
 Ackermann, M., Albert, A., Anderson, B., et al. 2014, *PhRvD*, **89**, 042001
 Albert, A., Anderson, B., Bechtol, K., et al. 2017, *ApJ*, **834**, 110
 An, D., Johnson, J. A., Clem, J. L., et al. 2008, *ApJS*, **179**, 326
 Astropy Collaboration, Robitaille, T. P., Tollerud, E. J., et al. 2013, *A&A*, **558**, A33
 Baltz, E., Berenji, B., Bertone, G., et al. 2008, *JCAP*, **0807**, 013
 Bechtol, K., Drlica-Wagner, A., Balbinot, E., et al. 2015, *ApJ*, **807**, 50
 Belokurov, V., Erkal, D., Deason, A. J., et al. 2017, *MNRAS*, **466**, 4711
 Belokurov, V., & Koposov, S. E. 2016, *MNRAS*, **456**, 602
 Belokurov, V., Walker, M. G., Evans, N. W., et al. 2008, *ApJL*, **686**, L83
 Besla, G., Martínez-Delgado, D., van der Marel, R. P., et al. 2016, *ApJ*, **825**, 20
 Bonnavard, V., Combet, C., Daniel, M., et al. 2015a, *MNRAS*, **453**, 849
 Bonnavard, V., Combet, C., Maurin, D., & Walker, M. G. 2015b, *MNRAS*, **446**, 3002
 Boubert, D., Erkal, D., Evans, N. W., & Izzard, R. G. 2017, *MNRAS*, **469**, 2151
 Bressan, A., Marigo, P., Girardi, L., et al. 2012, *MNRAS*, **427**, 127
 Carrera, R., Pancino, E., Gallart, C., & del Pino, A. 2013, *A&A*, **558**, A33
 Charles, E., Sánchez-Conde, M., Anderson, B., et al. 2016, *PhR*, **636**, 1
 Cooper, M. C., Newman, J. A., Davis, M., Finkbeiner, D. P., & Gerke, B. F. 2012, spec2d: DEEP2 DEIMOS Spectral Pipeline, Astrophysics Source Code Library, ascl:1203.003
 Deason, A. J., Wetzel, A. R., Garrison-Kimmel, S., & Belokurov, V. 2015, *MNRAS*, **453**, 3568
 de Jong, J. T. A., Martin, N. F., Rix, H.-W., et al. 2010, *ApJ*, **710**, 1664
 D'Onghia, E., & Lake, G. 2008, *ApJL*, **686**, L61
 Dooley, G. A., Peter, A. H. G., Carlin, J. L., et al. 2017, *MNRAS*, **472**, 1060
 Dressler, A., Bigelow, B., Hare, T., et al. 2011, *PASP*, **123**, 288
 Dressler, A., Hare, T., Bigelow, B. C., & Osip, D. J. 2006, *Proc. SPIE*, **6269**, 62690F
 Drlica-Wagner, A., Albert, A., Bechtol, K., et al. 2015a, *ApJL*, **809**, L4
 Drlica-Wagner, A., Bechtol, K., Allam, S., et al. 2016, *ApJL*, **833**, L5
 Drlica-Wagner, A., Bechtol, K., Rykoff, E. S., et al. 2015b, *ApJ*, **813**, 109
 Duffau, S., Zinn, R., Vivas, A. K., et al. 2006, *ApJL*, **636**, L97
 Eadie, G. M., & Harris, W. E. 2016, *ApJ*, **829**, 108
 Evans, N. W., Sanders, J. L., & Geringer-Sameth, A. 2016, *PhRvD*, **93**, 103512
 Evslin, J. 2014, *MNRAS*, **440**, 1225
 Feroz, F., & Hobson, M. P. 2008, *MNRAS*, **384**, 449
 Feroz, F., Hobson, M. P., & Bridges, M. 2009, *MNRAS*, **398**, 1601
 Flaugh, B., Diehl, H. T., Honscheid, K., et al. 2015, *AJ*, **150**, 150
 Foreman-Mackey, D. 2016, *JOSS*, **1**, 24
 Garrison-Kimmel, S., Boylan-Kolchin, M., Bullock, J. S., & Kirby, E. N. 2014, *MNRAS*, **444**, 222
 Genina, A., & Fairbairn, M. 2016, *MNRAS*, **463**, 3630
 Geringer-Sameth, A., Koushiappas, S. M., & Walker, M. 2015a, *ApJ*, **801**, 74
 Geringer-Sameth, A., Walker, M. G., Koushiappas, S. M., et al. 2015b, *PhRvL*, **115**, 081101
 Hayashi, K., Ichikawa, K., Matsumoto, S., et al. 2016, *MNRAS*, **461**, 2914
 He, C., Bechtol, K., Hearin, A. P., & Hooper, D. 2015, *PhRvD*, **91**, 063515
 Jeltema, T. E., & Profumo, S. 2008, *JCAP*, **11**, 003
 Jethwa, P., Erkal, D., & Belokurov, V. 2016, *MNRAS*, **461**, 2212
 Ji, A. P., Frebel, A., Simon, J. D., & Geha, M. 2016, *ApJ*, **817**, 41
 Kim, D., Jerjen, H., Geha, M., et al. 2016, *ApJ*, **833**, 16
 Kim, D., Jerjen, H., Mackey, D., Da Costa, G. S., & Milone, A. P. 2015, *ApJL*, **804**, L44
 Kirby, E. N., Cohen, J. G., Guhathakurta, P., et al. 2013, *ApJ*, **779**, 102
 Kirby, E. N., Cohen, J. G., Simon, J. D., et al. 2017, *ApJ*, **838**, 83
 Kirby, E. N., Cohen, J. G., Simon, J. D., & Guhathakurta, P. 2015a, *ApJ*, **814**, L7
 Kirby, E. N., Simon, J. D., & Cohen, J. G. 2015b, *ApJ*, **810**, 56
 Koch, A., Wilkinson, M. I., Kleyna, J. T., et al. 2009, *ApJ*, **690**, 453
 Koposov, S. E., Belokurov, V., Torrealba, G., & Evans, N. W. 2015, *ApJ*, **805**, 130
 Layden, A. C. 1994, *AJ*, **108**, 1016
 Li, T. S., Simon, J. D., Drlica-Wagner, A., & Bechtol, K. 2017, *ApJ*, **838**, 8
 Mackey, A. D., Koposov, S. E., Erkal, D., et al. 2016, *MNRAS*, **459**, 239
 MacQueen, J. 1967, in Proc. Fifth Berkeley Symp. Mathematical Statistics and Probability 1, Statistics (Berkeley, CA: Univ. California Press), 281
 Martínez, G. D., Bullock, J. S., Kaplinghat, M., Strigari, L. E., & Trotta, R. 2009, *JCAP*, **6**, 14
 Mattox, J., Bertsch, D., Chiang, J., et al. 1996, *ApJ*, **461**, 396
 McMillan, P. J. 2011, *MNRAS*, **414**, 2446
 Muñoz, R. R., Majewski, S. R., Zaggia, S., et al. 2006, *ApJ*, **649**, 201
 Navarro, J. F., Frenk, C. S., & White, S. D. M. 1996, *ApJ*, **462**, 563
 Nidever, D. L., Majewski, S. R., & Butler Burton, W. 2008, *ApJ*, **679**, 432
 Nidever, D. L., Majewski, S. R., Butler Burton, W., & Nigra, L. 2010, *ApJ*, **723**, 1618
 Nidever, D. L., Olsen, K., Walker, A. R., et al. 2017, *AJ*, **154**, 199
 Oemler, A., Clardy, K., Kelson, D., Walth, G., & Villanueva, E. 2017, COSMOS: Carnegie Observatories System for MultiObject Spectroscopy, Astrophysics Source Code Library, ascl:1705.001
 Oke, J. B. 1966, *ApJ*, **145**, 468
 Pace, A. B., & Strigari, L. E. 2018, arXiv:1802.06811
 Pasquini, L., Avila, G., Allaert, E., et al. 2000, *Proc. SPIE*, **4008**, 129
 Plummer, H. C. 1911, *MNRAS*, **71**, 460
 Read, J. I., Wilkinson, M. I., Evans, N. W., Gilmore, G., & Kleyna, J. T. 2006, *MNRAS*, **367**, 387
 Robin, A. C., Reylé, C., Derrière, S., & Picaud, S. 2003, *A&A*, **409**, 523
 Sales, L. V., Navarro, J. F., Cooper, A. P., et al. 2011, *MNRAS*, **418**, 648
 Sales, L. V., Navarro, J. F., Kallivayalil, N., & Frenk, C. S. 2017, *MNRAS*, **465**, 1879
 Sanders, J. L., Evans, N. W., Geringer-Sameth, A., & Dehnen, W. 2016, *PhRvD*, **94**, 063521
 Schlegel, D. J., Finkbeiner, D. P., & Davis, M. 1998, *ApJ*, **500**, 525
 Schönrich, R., Binney, J., & Dehnen, W. 2010, *MNRAS*, **403**, 1829
 Sharp, R., Saunders, W., Smith, G., et al. 2006, *Proc. SPIE*, **6269**, 62690G
 Simon, J. D., Drlica-Wagner, A., Li, T. S., et al. 2015, *ApJ*, **808**, 95
 Simon, J. D., & Geha, M. 2007, *ApJ*, **670**, 313
 Simon, J. D., Li, T. S., Drlica-Wagner, A., & Bechtol, K. 2017, *ApJ*, **838**, 11
 Sohn, S. T., Majewski, S. R., Muñoz, R. R., et al. 2007, *ApJ*, **663**, 960

⁴² PARSEC isochrones at <http://stev.oapd.inaf.it/cgi-bin/cmd>.

⁴³ Details of the DECam system response and filter throughput are available at the CTIO website <http://www.ctio.noao.edu/noao/node/1033>. The specific system response file used to compute the new isochrones is available at http://www.ctio.noao.edu/noao/sites/default/files/DECam/DECam_filters.xlsx.

⁴⁴ All photometry presented in this paper is corrected for interstellar extinction using the extinction map from Schlegel et al. (1998). The $E(B - V)$ value around Car II and Car III is around 0.19.

- Steigman, G., Dasgupta, B., & Beacom, J. F. 2012, [PhRvD](#), **86**, 023506
- Strigari, L. E., Koushiappas, S. M., Bullock, J. S., et al. 2008, [ApJ](#), **678**, 614
- Torrealba, G., Belokurov, V., Koposov, S. E., et al. 2018, *MNRAS*, arXiv:1801.07279
- van der Marel, R. P., Alves, D. R., Hardy, E., & Suntzeff, N. B. 2002, [AJ](#), **124**, 2639
- van der Marel, R. P., & Kallivayalil, N. 2014, [ApJ](#), **781**, 121
- van der Marel, R. P., Kallivayalil, N., & Besla, G. 2009, in *IAU Symp.* 256, *The Magellanic System: Stars, Gas, and Galaxies*, ed. J. T. Van Loon & J. M. Oliveira (Cambridge: Cambridge Univ. Press), 81
- van der Marel, R. P., & Sahlmann, J. 2016, [ApJL](#), **832**, L23
- van Dokkum, P. G. 2001, [PASP](#), **113**, 1420
- Vivas, A. K., Jaffé, Y. L., Zinn, R., et al. 2008, [AJ](#), **136**, 1645
- Vivas, A. K., Zinn, R., & Gallart, C. 2005, [AJ](#), **129**, 189
- Walker, M. G., Belokurov, V., Evans, N. W., et al. 2009a, [ApJL](#), **694**, L144
- Walker, M. G., Combet, C., Hinton, J. A., Maurin, D., & Wilkinson, M. I. 2011, [ApJL](#), **733**, L46
- Walker, M. G., Mateo, M., Olszewski, E. W., et al. 2006, [AJ](#), **131**, 2114
- Walker, M. G., Mateo, M., Olszewski, E. W., et al. 2009b, [ApJ](#), **704**, 1274
- Walker, M. G., Mateo, M., Olszewski, E. W., et al. 2016, [ApJ](#), **819**, 53
- Wheeler, C., Pace, A. B., Bullock, J. S., et al. 2017, *MNRAS*, **465**, 2420
- Winter, M., Zaharijas, G., Bechtol, K., & Vandenbroucke, J. 2016, [ApJL](#), **832**, L6
- Wolf, J., Martinez, G. D., Bullock, J. S., et al. 2010, *MNRAS*, **406**, 1220
- Yanny, B., Newberg, H. J., Johnson, J. A., et al. 2009, [ApJ](#), **700**, 1282
- Zacharias, N., Finch, C. T., Girard, T. M., et al. 2013, [AJ](#), **145**, 44